HHS Public Access

Author manuscript

Nat Aging. Author manuscript; available in PMC 2024 August 14.

Published in final edited form as:

Nat Aging. 2021 October ; 1(10): 889–903. doi:10.1038/s43587-021-00103-w.

Escape of hair follicle stem cells causes stem cell exhaustion during ageing

Chi Zhang[1,6], **Dongmei Wang**[1,6], **Jingjing Wang**[1,6], **Li Wang**[2], **Wenli Qiu**[4], **Tsutomu Kume**[5], **Robin Dowell**[1,3], **Rui Yi**[1,6,*]

[1]Department of Molecular, Cellular and Developmental Biology, University of Colorado Boulder, Boulder, CO USA 80309

[2]10x Genomics, 7068 Koll Center Parkway, Pleasanton, CA USA 94566

[3]BioFrontiers Institute, University of Colorado Boulder, Boulder, CO USA 80309

[4]Lung Biology Center, Department of Medicine, UCSF, San Francisco, CA USA 94158

[5]Feinberg Cardiovascular and Renal Research Institute, Northwestern University Feinberg School of Medicine, Chicago IL USA 60611

[6]Present address: Department of Pathology, Department of Dermatology, Northwestern University Feinberg School of Medicine, Chicago, IL USA 60611

Abstract

Stem cell (SC) exhaustion is a hallmark of ageing. However, the process of SC depletion during ageing has not been observed in live animals, and the underlying mechanism contributing to tissue deterioration remains obscure. We find that, in aged mice, epithelial cells escape from hair follicle SC (HF-SC) compartment to the dermis, contributing to HF miniaturization. Single-cell RNA-seq and ATAC-seq reveals the reduced expression of cell adhesion and extracellular matrix genes in aged HF-SCs, many of which are regulated by *Foxc1* and *Nfatc1*. Deletion of *Foxc1* and *Nfatc1* recapitulates HF miniaturization and causes hair loss. Live imaging captures individual epithelial cells migrating away from the SC compartment and HF disintegration. This study illuminates a hitherto unknown activity of epithelial cells escaping from their niche as a mechanism underlying SC reduction and tissue degeneration. Identification of homeless epithelial cells in aged tissues provides a new perspective for understanding ageing-associated diseases.

Ageing is defined as functional decline of tissues and organisms, and contributes to many human diseases including cancer and neurodegenerative diseases[1,2]. Although it is widely recognized that stem cell (SC) exhaustion is a hallmark of ageing[2], cellular activities of

*Correspondence: yir@northwestern.edu.

Author Contribution Statement

R.Y. conceived the study. C.Z., D.W. and R.Y. designed the experiments. C.Z. carried out most experiments and computational analysis with assistance from D.W. for immunofluorescence staining and imaging. J. Wang performed two-photon imaging for some control experiments. L.W. helped to analyze scATAC-seq data. W.Q. generated Itgb6 KO mouse and provided samples. T.K. generated Foxc1 mouse models. R.D. supervised computational analysis. R.Y. and R.D. were co-mentors to C.Z. R.Y. wrote the manuscript with input from all authors.

Competing Interests statement

The authors declare no competing interests.

tissue SCs during ageing have been rarely observed in their intact microenvironment[3,4]. It remains largely unknown how tissue SCs divide, migrate and perish during ageing. Without a clear picture of these fundamental cellular behaviors, current knowledge of tissue SC ageing has been acquired through indirect measurement of SC numbers and functions[5–10]. As a result, our understanding of SC exhaustion is largely limited to the deficiency of cell division and self-renewal, usually caused by DNA damage and cellular senescence[8,11–13].

Among fundamental properties of tissue SCs, quiescence is known to play an important role in SC maintenance by restricting the number of SC divisions and reducing cellular stress[14–17]. Although the loss of quiescence has been shown to cause the lost proliferative potential of SCs in a cell-intrinsic manner[18,19], SC activities have not been visualized when they lose quiescence. Furthermore, it is unclear whether the loss of SC quiescence affects the integrity of SC compartment independently of cell division control. Finally, SC division rates generally decrease during ageing[20], it remains an open question how prolonged SC quiescence affects ageing.

Hair follicle (HF) of mammalian skin is an excellent experimental system to examine cellular activities and molecular networks of largely quiescent SC populations during ageing. HF loss and graying has been widely recognized as macroscopic signs of ageing both scientifically and culturally. At the cellular levels, HF miniaturization has been reported to associate with hair loss during ageing[8] and alopecia caused by premature hair loss[21,22]. In these studies, cell apoptosis as a result of accumulated DNA damage or altered signaling pathways, which are critical for hair growth, are identified as underlying mechanisms of SC exhaustion or compromised hair growth, respectively. However, hair follicle SCs (HF-SCs) and their activities have not been examined in live animals during ageing.

In this study, we use noninvasive intravital imaging and single-cell genomic tools to measure multiple modalities of HF-SCs including cellular activities, transcriptome and open chromatin landscape in aged HFs. Surprisingly, we observe that numerous epithelial cells, many of them located near the bulge SC compartment, escape to the dermis during ageing. We characterize the reduced expression of cell adhesion and extracellular matrix (ECM) genes as a prominent feature of aged HF-SCs, and identify *Foxc1* and *Nfatc1* as key regulators of HF-SC-specific cell adhesion. Deletion of these two genes recapitulates epithelial cell escape, leads to rapid HF miniaturization and hair loss. Our study reveals SC escape as a new mechanism for SC reduction and tissue degeneration.

Results

Escaped epithelial cells in aged hair follicles

To visualize HF-SC compartment in live animals during ageing, we used two-photon intravital imaging to observe H2bGFP labeled (*Krt14-H2bGFP*) epithelial cells in HFs[23,24] in both young (~6–8mo old) and old (>20mo old) mice. In young mice, the HF-SC compartment was readily distinguished by the convex morphology of the bulge region, which is located below the morphologically distinct sebaceous gland (SG), and epithelial cells were restricted within the cylinder of HFs regardless of hair cycle stages (Fig. 1a and Extended Data Fig. 1a). In contrast, miniaturized HFs, which are characterized by

reduced cellularity, shrinking bulge compartment and the upward movement of the HF-SC compartment toward the SGs, were frequently observed in old mice (Fig. 1a). In some of these HFs, individual H2bGFP+ epithelial cells were located outside of the typical HF cylinder but in a close proximity to the HF (Fig. 1a and Extended Data Fig. 1b). We also used second-harmonic-generation (SHG) imaging of dermal collagen fiber and confirmed the localization of these H2bGFP+ epithelial cells in the dermis (Fig. 1b). We therefore referred these cells as escaped epithelial cells.

We next quantified the size of HF-SC compartment of telogen HFs in young and old mice (see online Methods). We observed the gradual but statistically significant reduction of the size of HF-SC compartment in old mice (Fig. 1c). Overall, ~14.5% of HF-SC compartment was miniaturized (defined by the smaller size than the smallest HF-SC compartment in young mice) in ~20mo old animals (Fig. 1c and Extended Data Fig. 1c). Furthermore, ~5.8% of aged HFs contained escaped H2bGFP+ epithelial cells near the HF-SC compartment (Fig. 1d). HFs with escaped epithelial cells were also significantly smaller than HFs without escaped cells (Fig. 1e). We have also examined apoptotic cells within HF-SC compartment, which were previously shown to contribute to HF miniaturization[8]. On average, we observed ~4.8% of aged HFs containing apoptotic HF-SCs marked by activated caspase3, within the bulge region and ~4.8% within the HGs. We also observed ~3.8% of young HFs containing apoptotic HF-SCs within the bulge region and ~5.8% within the HGs (Extended Data Fig. 1d–f). These data suggest that the number of apoptotic cells, as detected by activated caspase3, do not differ drastically in young and old mice.

To examine the relationship between epithelial cell escape and HF miniaturization, we longitudinally tracked the same HFs, which usually rested in the quiescent telogen phase, in live animals. In most frequently observed cases, we first observed signs of loosely organized epithelial cells in the bulge region in contrast to the stereotypical morphology of tightly packed HF-SC compartment in normal HFs. In ~10 days, these HFs lost some loosely organized epithelial cells and became smaller (Fig. 1f). In some rare but more rapidly progressing cases, we observed numerous H2bGFP+ epithelial cells scattering around miniaturizing HFs. Within a few days, these H2bGFP+ cells spread from the HF to neighboring regions or reached deeper regions of the dermis (Fig. 1g and Extended Data Fig. 1g). In about 2 weeks, however, most of these scattered cells were no longer visible, and the miniaturizing HF was rapidly degenerated (Fig. 1g). We further confirmed the epithelial identity of these scattered cells in the dermis as Krt5+/Vim- and Krt5+/Sox9+ cells in aged mice (Fig. 1h–i and movie S1). Escape of epithelial cells away from the bulge to the dermis suggests compromised basement membrane (BM). Indeed, we observed HF-SCs in the bulge region protruding toward the dermis with immunofluorescence (IF) staining of β4 integrin, a BM marker, in old mice (Extended Data Fig. 1h). These data reveal an unexpected activity of epithelial cells escaping to the dermis in aged HFs, and establish a correlation between epithelial cell escape and HF miniaturization during ageing (Fig. 1j).

Reduced cell adhesion in aged HF-SCs

We next applied single-cell RNA-seq (scRNA-seq) to examine cellular states of skin epithelial cells isolated from young and old mice. HFs experience increasingly long telogen

phase and much less frequent anagen growth in old mice, and by 18 to 24 months most HFs enter extended telogen, often lasting more than 100 days[25]. Therefore, we profiled the telogen phase as the representative hair cycle stage in young mice at postnatal day 53 (P53), the middle of the second telogen, and in old mice at 24 months (24mo), which showed typical signs of ageing such as hair thinning and occasionally gray hair. After quality control, we detected 3,524 epithelial cells in the P53 sample and 2,881 epithelial cells in the 24mo sample (Extended Data Fig. 2a and online Methods). We aggregated both young and old samples together and applied UMAP (Uniform Manifold Approximation and Projection for Dimension Reduction) to detect cell lineage dynamics and changes in the transcriptome[26]. Overall, three well-characterized, spatially distinct epithelial cell lineages including interfollicular epidermal (IFE) lineages, infundibular (IFN) and sebaceous gland (SG) lineages, and HF lineages were identified in both samples (Fig. 2a and Extended Data Fig. 2b–c). The projection of each lineage and individual cell clusters from young and old samples largely overlapped. To gain deeper insights into the different cellular states at a higher resolution, we re-clustered IFE and HF cells of young and old samples. Notably, epithelial cells of HF-SC compartment from young mice were readily resolved into two distinct populations corresponding to outer bulge HF-SCs and inner bulge niche cells, marked by Krt24 and Fgf18, respectively (Fig. 2b–c). In contrast, the demarcation of these two distinct populations was greatly reduced in the old sample (Fig. 2b–c), a trend similar to altered cellular states of fibroblasts during ageing[27]. Interestingly, although basal cells of IFE showed different cellular states between young and old samples, differentiated suprabasal cells from young and old samples clustered together (Extended Data Fig. 3a–d).

We next performed differential gene expression analysis for HF-SCs and IFE basal cells between young and old samples. The most significantly downregulated genes in old HF-SCs were enriched in gene ontology (GO) terms such as regulation of cell adhesion, response to wounding, cell junction assembly and extracellular matrix (ECM) (Fig. 2d and Supplementary Table 1). Upregulated genes in old HF-SCs were enriched for transcription factor (TF) AP1 complex and apoptotic signaling pathway (Extended Data Fig. 3e and Supplementary Table 2). The most enriched GO categories in downregulated genes from old basal IFE progenitors were MHC class I peptide loading complex, response to wounding and negative regulation of cell differentiation (Extended Data Fig. 3f). The specificity of downregulated cell adhesion and ECM genes in old HF-SCs was further supported by examining individual genes. For example, *Actg1* and *Itgb6* are widely expressed genes in both HF-SCs and IFE basal cells but were only downregulated in old HF-SCs but not IFE (Fig. 2e and Extended Data Fig. 3g). Nephronectin (*Npnt*), an HF-SC specific ECM gene[28], was only detectable in HF-SCs and downregulated in the old (Fig. 2e and Extended Data Fig. 3g). In contrast, *Jun* and *Junb*, both of AP1 TFs, were upregulated in both HF-SCs and IFE of old mice.

We performed pseudotime analysis using monocle3[29] to examine lineage progression. It recapitulated the differentiation trajectory of distinct HF lineages in both young and old samples (Extended Data Fig. 3h). Interestingly, we observed a differential distribution of young and old HF-SCs along the pseudotime trajectory (Extended Data Fig. 3i). Young HF-SCs clustered in a more ground state, which is characterized by elevated gene expression in adherens junction, tissue morphogenesis and regulation of cell adhesion. In contrast,

many more old HF-SCs clustered in a more differentiated state, which is characterized by less cell adhesion (Extended Data Fig. 3j). These data reveal the reduction of cell adhesion and ECM gene expression specifically in aged HF-SCs.

Downregulation of *Foxc1* and *Nfatc1* in aged HF-SCs

To probe transcriptional mechanism that underlies the reduced gene expression during ageing, we identified several enriched TF motifs in HF-SC-specific open chromatin regions, determined by ATAC-seq, that surround the downregulated genes in aged HF-SCs (Fig. 3a). Because aged HFs largely rested in extended telogen[25], the enrichment of ETS/RUNX motifs, which are generally associated with activated HF-SCs[30,31], was consistent with the lack of anagen HF growth. However, it was paradoxical that TFs promoting quiescence, including NFATC1, FOXC1 and TCF7L2[7,10,32–34], were associated with downregulated genes in largely quiescent HF-SC populations in aged mice. To examine this issue, we monitored the transcriptional activity of the *Foxc1* locus by using *Foxc1-LacZ* knock-in mice in middle-aged mice (~15-mo old). In these mice, most HFs were rested in telogen but some HFs were still infrequently cycling and in anagen. We observed the absence of LacZ signals in the quiescent HF-SCs located within the telogen bulge but robust LacZ signals in the bulge regions of anagen HFs (Extended Data Fig. 4a–c). Furthermore, IF staining and quantification confirmed the reduced expression of FOXC1 in aged HF-SCs located within the telogen bulge (Fig. 3b). Of note, *Foxc1* expression in the upper HF and SGs, determined by both *Foxc1-LacZ* and IF signals, was not changed (Fig. 3b and Extended Data Fig. 4), reflecting HF-SC-specific *Foxc1* downregulation. In addition, NFATC1 expression was also slightly downregulated in aged HF-SCs (Fig. 3c). We have previously shown that *Foxc1* are induced in dividing HF-SCs during the anagen phase and *Foxc1* promotes the expression of *Nfatc1* and Bmp[10]. Thus, the prolonged telogen diminishes the expression of *Foxc1* in aged HF-SCs, likely due to the lack of anagen activation.

We next performed bulk RNA-seq to identify genes that are downregulated in *Foxc1* conditional knockout (cKO) *(Krt14-Cre/Foxc1$^{fl/fl}$)* and *Nfatc1* cKO *(Krt14-Cre/Nfatc1$^{fl/fl}$)* HF-SCs, respectively. Interestingly, cell adhesion, ECM and BM genes were top enriched GO categories for each cKO, in addition to well-appreciated regulation of signaling pathways such as Bmp and Fgf and the regulation of proliferation (Fig. 3d–e and Supplementary Table 3–4). We further compared these downregulated genes to a published bulk RNA-seq dataset from aged HF-SCs[6], and identified a number of cell adhesion and ECM genes, such as *Ltbp1, Ctgf, Itgb6* and *Vwa2,* that are commonly downregulated in the HF-SCs between aged mice and *Foxc1* or *Nfatc1* cKO (Fig. 3f). Interestingly, we also identified genes prominently associated with HF-SC quiescence, such as *Peg3*, *Cd34, Fgf18, Nog* and *Tle4*[7,10,34–37], that are commonly downregulated in aged and cKO HF-SCs (Supplementary Table 5). These downregulated cell adhesion and ECM genes harbored many open chromatin regions containing FOXC1 and NFATC1 motifs within or near their loci (Fig. 3g). These data lend further support to a link between reduced *Foxc1* and *Nfatc1* expression and the ageing of HF-SCs. Our analysis also reveals that extended quiescence of aged HF-SCs diminishes the expression of *Foxc1.*

Loss of *Foxc1* and *Nfatc1* causes premature ageing

To test the function of *Foxc1* and *Nfatc1* during ageing, we deleted both TFs in the skin using *Krt14-Cre* (*Krt14-Cre/Foxc1*$^{fl/fl}$*/Nfatc1*$^{fl/fl}$), hereafter termed double knockout (dKO) (Fig. 4a). In young mice, we observed strongly compromised HF-SC quiescence as indicated by widespread Ki67 signals in HF-SCs in Anagen I (P22), Anagen III (P25), and the second telogen (P42) (Fig. 4b–c and Extended Data Fig. 5a). In contrast, HF-SCs in control animals were only in the active cell cycle transiently, mostly in the early to middle anagen (Extended Data Fig. 5a), consistent with the notion that HF-SCs are largely quiescent and infrequently divide for self-renewal[38,39]. Furthermore, strong Ki67 signals were observed in the HF-SCs of dKO but not *Foxc1* or *Nfatc1* single cKO by late anagen (Extended Data Fig. 5b), indicating a synergistic effect of deleting *Foxc1* and *Nfatc1* in quiescence. At the tissue scale, young dKO mice rapidly regenerated their hair coat in less than 2 weeks after shaving, in sharp contrast to control (Extended Data Fig. 5c).

Despite robust hair regeneration in young mice, dKO animals began to show signs of hair loss by ~5-month old (Fig. 4d). By 12–16 months, dKO animals largely lost their hair coat and the remaining hair turned gray while they were otherwise healthy and had a normal lifespan (Fig. 4e and Extended Data Fig. 5d). We first examined whether compromised HF-SC quiescence led to the loss of proliferative potential of HF-SCs in dKO, as one may predict. However, we observed numerous Ki67+ proliferative cells in the HF-SC compartment of both growing and resting HFs in 16mo old dKO mice when hair loss was widespread (Fig. 4f). We then used intravital imaging to directly monitor the dynamics of hair growth and loss in dKO animals. Strikingly, we observed many growing, anagen HFs, which reflect robust HF growth, despite widespread hair loss. However, we also observed numerous miniaturized HFs concurrently in the same dKO animals. Some HFs reduced to a few remaining cells and were progressing toward the complete degeneration (Fig. 4g and Extended Data Fig. 5e). Unlike control HFs that typically clustered together with 2–4 HFs, which were usually in telogen, dKO HFs had irregular spacing, indicative of widespread but random HF loss as observed at the macroscopic level.

By examining the morphology of miniaturizing HFs, we found that many H2bGFP+ epithelial cells were located in the vicinity of HF-SC compartment but clearly outside of the HF cylinder (Fig. 4g and Extended Data Fig. 5e), recapitulating escaping epithelial cells as observed in aged HFs (see Fig. 1). We next quantified the size of telogen HF-SC compartment, the percentage of miniaturized HFs and the percentage of HFs containing escaped epithelial cells in dKO, and compared to young and aged mice (Fig. 4h–i and Extended Data Fig. 5f). On average, 12mo old dKO mice had 4.3 times more (77.3% vs 14.5%) miniaturized HFs than 20–24mo aged mice. The percentage of HFs containing escaped epithelial cells was 10.5% in dKO and 5.8% in aged mice. These results were consistent with the rapid progression of hair loss and premature HF ageing observed in dKO mice.

To monitor the process of HF degeneration in live animals, we longitudinally tracked the same HFs in dKO for multiple weeks. We observed that HF miniaturization and degeneration occurred invariably after the catagen-to-telogen transition. Notably, rather than forming the anatomically distinct bulge, miniaturizing HFs in dKO first showed signs of

abnormal cell egress in the bulge region (day 3 in Fig. 4j and movie S2). These escaping cells were transient and not observed in day 1 or 5 or any time points other than day 3. The HF then regressed to a loosely packed epithelial strand, which lacked the convex morphology (day 9 in Fig. 4j), mimicking many miniaturized HFs observed in aged skin. In ~3 weeks, these dKO HFs became further miniaturized until the complete degeneration with less than 5 cells left in the HF (day 26 in Fig. 4j). To determine the correlation between HF miniaturization and the number of HF-SCs, we quantified the number of HF-SCs in telogen HFs directly in live animals. The number of HF-SCs per HF were significantly reduced in old mice and even more so in dKO mice (Extended Data Fig. 5g–h).

In addition to these rapidly dying HFs, however, we also observed many HFs that go through the hair cycle and continuously regenerate in the same animals (Extended Data Fig. 5i). Notably, these HFs did not shown sign of epithelial cell escape and continued to cycle within our observation window. Thus, the appearance of escaping epithelial cells from the bulge region distinguished the miniaturizing HFs from continuously cycling HFs in dKO. Overall, we have tracked 78 individual HFs over the span of at least 16 days. We found 62.8% of HFs undergoing regeneration, 26.9% undergoing miniaturization and degeneration, and 9.0% remaining quiescence (Extended Data Fig. 5j).

These live imaging data reveal the dynamics of HF-SC loss accompanying by HF miniaturization. They suggest that the loss of HF-SCs through cell escape rather than enhanced HF-SC proliferation or compromised proliferative potential is correlated with SC exhaustion in dKO.

Reduced expression of cell adhesion and ECM genes

We next performed scRNA-seq to examine changes of gene expression in control and dKO samples at P38, when HFs are in the late anagen, and HF-SCs return to quiescence[10]. Similar to aged skin, cell clusters of epithelial cell populations did not change drastically, judging by the UMAP projection (Fig. 5a and Extended Data Fig. 6a–c). Notably, genes involved in the regulation of cell adhesion and negative regulation of cell proliferation were among the most enriched in the downregulated genes in dKO HF-SCs (Fig. 5b and Supplementary Table 6). Among them, many of them are commonly downregulated in aged HF-SCs such as *Actg1, Cd34, Itgb6* and *Npnt.*

To examine the specificity of *Foxc1* and *Nfatc1*-mediated regulation in HF-SCs, we used *Krt15-CrePR* to delete *Foxc1* and *Nfatc1* only in the HF-SC compartment starting at P22 (Extended Data Fig. 7a) and purified dKO HF-SCs for bulk RNA-seq at P30. In support of the notion that these two TFs govern HF-SC gene expression in a cell-intrinsic manner, a large number of genes, which were downregulated in *Foxc1* and *Nfatc1* single cKO, were also downregulated in the induced dKO (Fig. 5c–d and Supplementary Table 7). Because the induced dKO only deleted both TFs shortly before sample collection, nearly all of these genes were more mildly downregulated in induced dKO than in either single cKO, which deleted each TF at the beginning of skin development with *Krt14-Cre* (Fig. 5d). Consistent with the scRNA-seq data, the most highly enriched gene categories that were downregulated in induced dKO HF-SCs were cell adhesion, negative regulation of cell proliferation and ECM genes (Fig. 5e). Among cell adhesion and ECM genes that were downregulated,

Igfbp5, *Ctgf, Postn, Ltbp2, Col6a1, Npnt* and *Egfl6* are highly enriched in HF-SCs[28]. Among upregulated genes, the strongest elevation of gene expression was associated with mitotic cell cycle and cytokinesis in dKO HF-SCs (Extended Data Fig. 7b).

We next examined the expression of several cell adhesion and ECM genes including *Npnt, Cd34* and *Egfl6* in dKO and aged animals. At P42 when dKO HFs were in the telogen phase morphologically, the signals of NPNT, CD34 and EGFL6 were all significantly reduced. In particular, CD34 was not detectable (Fig. 5f). In 24mo old sample, NPNT and CD34 but not EGFL6 were also reduced (Fig. 5f–g). Interestingly, the expression of NPNT, an ECM protein that is localized to the BM of the bulge and HG[28], was lost specifically in the bulge HF-SCs but not in HG of both dKO and old samples (Fig. 5f), further supporting HF-SC-specific control of *Npnt* by *Foxc1* and *Nfatc1*. We next confirmed that CD34 was absent in *Krt14-Cre/Foxc1*$^{fl/fl}$*/Nfatc1*$^{fl/fl}$ dKO HF-SCs at P30 by using FACS (Extended Data Fig. 7c–d). In comparison, CD34 was expressed at a lower but still detectable level in both *Foxc1* and *Nfatc1* single cKO HF-SCs (Extended Data Fig. 7e). Furthermore, in *Krt15-CrePR* induced dKO, CD34 level was also downregulated but not completely lost 8 days after the induction of deletion (Extended Data Fig. 7f). These data suggest that *Cd34,* one of the most specific HF-SC surface markers and a cell adhesion gene[40–42], requires the combinatorial control of these two TFs (also see below). Despite the complete loss of CD34, however, dKO HF-SCs still maintained their fate as indicated by the robust expression of SOX9, a master TF governing the HF-SC fate[43–45] (Fig. 5h). In addition, dKO HFs continued to grow and cycle when they retain HF-SCs within the bulge (Extended Data Fig. 5i). Taken together, these analyses reveal that HF-SCs, in the absence of *Foxc1* and *Nfatc1,* have severely compromised cell adhesion and ECM gene expression, which resembled the downregulation of these genes during ageing.

Enhancer-promoter loops mediated by *Foxc1* and *Nfatc1*

To investigate how *Foxc1* and *Nfatc1* regulate HF-SC-specific cell adhesion and ECM gene expression, we next performed single-cell ATAC-seq (scATAC-seq) from control and dKO animals at P28. We detected the median of 19,512 fragments per cell in control and 17,392 fragments per cell in dKO. We clustered total epithelial cells using t-Distributed Stochastic Neighbor Embedding (t-SNE) technique based on open chromatin signatures determined by ATAC-seq[46,47] (Extended Data Fig. 8a). To validate whether scATAC-seq can correctly distinguish IFE and HF-SC lineages, we generated total open chromatin landscape of control IFE and HF-SC and compared them with bulk ATAC-seq datasets generated from FACS purified IFE[48] and HF-SC populations. Indeed, the open chromatin profile of IFE and HF-SC populations detected in scATAC-seq and bulk ATAC-seq was closely matched (Fig. 6a). We next examined enriched TF motifs in IFE- and HF-SC-specific open chromatin regions. We found GATA3/6, GRHL2/3, p63 and KLF motifs highly enriched in IFE-specific regions and LHX2, SOX9 and FOXC1 motifs highly enriched in HF-SC-specific regions (Fig. 6b), consistent with previous studies documenting the functions of these TFs in these epithelial lineages[7,10,45,49–53].

Next, we examined how the loss of *Foxc1* and *Nfatc1* affected open chromatin landscape by using aggregated scATAC-seq data. In support of the notion that *Foxc1* and *Nfatc1* are

specific to HF but not expressed in IFE cells, cellular states determined by open chromatin signatures revealed largely overlapping and similar populations of control and dKO IFE cells. Notably, cellular states of HF-SCs determined by open chromatin signatures were different between control and dKO (Fig. 6c), in contrast to our scRNA-seq results (Fig. 5a). These data indicate that scATAC-seq is more sensitive to cellular state changes than scRNA-seq, likely due to the much higher number of uniquely identified open chromatin regions than the number of genes detected in single cells. Indeed, we identified 3,980 open chromatin regions that were significantly reduced in dKO HF-SCs (Extended Data Fig. 8b). When we searched for the enrichment of TF motifs in these regions, we identified FOXC1 and NFATC1 motifs as the top 2 most highly enriched TFs (Extended Data Fig. 8c). Interestingly, we also found KLF4 motif as No. 3 most highly enriched.

We next examined how FOXC1 and NFATC1 co-regulate HF-SC-enriched cell adhesion and ECM genes. *Cd34* is one of the most specific markers for HF-SCs[40–42], and its expression was reduced in aged HF-SCs[8], in each of *Foxc1* and *Nfatc1* single cKO, and completely abolished in dKO (Fig. 5f and Extended Data Fig. 7d–f). Multiple FOXC1 and NFATC1 motif-containing open chromatin regions were identified at the *Cd34* locus (Fig. 6d). Interestingly, the transcription start site (TSS) and several enhancers of *Cd34* were uniquely open in HF-SCs but not IFE, mirroring the gene expression pattern in these two lineages. In dKO, a FOXC1 motif-containing site lost open chromatin signals, and the TSS and a NFATC1 motif-containing site also showed strongly reduced open chromatin signatures (Fig. 6d). Given the complete loss of CD34 expression in dKO, these data suggest that the open state of these FOXC1- and NFATC1-dependent enhancers is required for *Cd34* expression in HF-SCs. Similarly, *Actg1, Npnt, Col6a1* and *Col6a2* loci also contain FOXC1- and NFATC1-dependent, HF-SC-specific open chromatin regions (Extended Data Fig. 8d–f). Notably, *Actg1* is widely expressed in both IFE and HF-SCs (Extended Data Fig. 3g). However, a FOXC1-motif containing open chromatin region was robustly detected in control HF-SCs but not in dKO HF-SCs or IFE samples (Extended Data Fig. 8d). In support of the regulation of *Actg1* by FOXC1, *Actg1* was downregulated in old, *Foxc1* cKO and dKO HF-SCs but not in *Nfatc1* cKO HF-SCs or in old IFE. These data highlight the HF-SC-specific regulation for a widely expressed cell adhesion gene.

Recent studies demonstrate that scATAC-seq can provide insights into enhancer-promoter interactions by computing the co-accessibility of open chromatin regions in single cells[46,54]. We next examined the effect of FOXC1 and NFATC1 on local genome organization and enhancer-promoter interactions by computing Cicero co-accessibility[54]. Because cell adhesion and ECM genes such as *Actg1, Cd34, Col6a1, Itgb6, Npnt* and signaling genes such as *Bmp2* and *Fgf18* harbored FOXC1 and NFATC1 motif-containing enhancers and were strongly downregulated in dKO and aged HF-SCs, we examined enhancer-promoter interactions in their genomic loci. Enhancer-promoter interactions were generally sparse or absent for these genes in IFE cells, consistent with their HF-SC-specific expression. In contrast, many strong interactions were detected for these genes in control HF-SCs (Fig. 6e–f and Extended Data Fig. 9). A majority of these HF-SC-specific interactions, however, were compromised and the aggregated Cicero co-accessibility scores were reduced in dKO HF-SCs, correlating with their reduced gene expression. As control, the aggregated Cicero scores remained unchanged for *Krt14,* a highly expressed gene that is not affected

by dKO (Extended Data Fig. 9c). However, the score was different for *Krt14* in IFE and HF-SCs, perhaps reflecting different transcriptional controls of *Krt14* in these cell lineages. To determine TFs underlying the reduced enhancer-promoter interactions in the dKO, we searched the open chromatin regions with reduced Cicero scores. KLF4 motif was the most highly enriched followed by NFATC1 and FOXC1 motifs (Fig. 6g). These data reveal that *Foxc1* and *Nfatc1* control cell adhesion, ECM and signaling genes by promoting enhancer-promoter interactions specifically in HF-SCs.

Disintegration of HF-SC compartment in *Foxc1/Nfatc1* dKO

To visualize cellular activities underlying HF miniaturization and hair loss, we next examined HF-SCs using time-lapse imaging in dKO animals. In control skin, HFs mostly rested in the telogen phase, and HF-SCs were usually quiescent with miminum cellular activities within the imaging window of 4–6 hours (Fig. 7a and movie S3). Less frequently did we observe growing HFs in the anagen phase. In these HFs, we observed limited cell migration, mostly downward movement in the outer root sheath (ORS) compartment and upward movement in the inner root sheath (IRS) (movie S4). HF-SCs were mostly immobile, and we occasionally observed HF-SC migration but generally no cell division observed within the window of 4–6 hours (Fig. 7b and movie S4). In dKO skin, however, we routinely found numerous growing HFs. ORS progenitors in dKO mice rapidly migrated, mostly moving along the outer surface of HF laterally or downwardly (movie S5). We also observed strong activities of cells migrating away from the HF-SC compartment. In a 4-hour imaging session, we observed an HF-SC detached from neighboring cells and crawled along the HF. In the same HF, two HF-SCs escaped from the bulge region to the dermis. Strikingly, we observed these two cells simultaneously changed the shape of their nuclei (24–108 min images of Fig. 7c) and squeezed through likely a small orifice on the BM before migrating away separately (Fig. 7c and movie S6). Most notably, one of these two escaping cells “jumped” more than 16μm away from the HF in less than 30min after the initial escape, further ruling out the possibility that it remained within the HF (Fig. 7c). These data documented the rapid escape of individual epithelial cells from the HF-SC compartment to the dermis, likely as a result of compromised cell adhesion and defective BM. In support, we detected individual dKO HF-SCs with strongly reduced β4 integrin signals by IF staining (Fig. 7d). These time-lapse movies thus provided direct evidence that dKO HF-SCs are a source of H2bGFP+ epithelial cells that have escaped from dKO HFs (Fig. 4g, 4j and 7c). Although it appeared to be random when an HF lost cells from the SC compartment into the dermis, their occurrence was generally associated with subsequent HF miniaturization and hair loss as documented in figure 4j.

To monitor the degeneration of HF-SC compartment, we visualized miniaturized HFs prior to the complete HF loss. Although cell migration and division were relatively infrequent, we still observed cell division activities in these miniaturized HFs. In a miniaturized HF, we simultaneously observed a cell division event, three nearby cells disintegrating and releasing into the dermis, and one escaped cell migrating in the dermis within the span of 2½ hours (Fig. 7e and movie S7). In another miniaturized HF that contains less than 20 cells, one epithelial cell moved downward and were poised to escape from the HF (movie S8). These data suggest that miniaturized HFs are still capable of cell division but continue to lose

epithelial cells due to cell escape. Although we were unable to image the fate of these escaped cells due to the limitation of imaging protocol in live animals, they usually scattered around the dying HFs while other HFs continued to shed epithelial cells (Fig. 7f and movie S9). These cellular activities recapitulated the escaped HF-SCs observed from aged HFs (Fig. 1a–b and f-g), indicating that cell escape is a common mechanism.

To test whether the loss of individual cell adhesion and ECM genes may recapitulate cell escape and premature ageing, we genetically deleted *Itgb6,* which is commonly downregulated in both aged and dKO HF-SCs and controlled by *Foxc1* and *Nfatc1.* Although genetic deletion of *Itgb6* was reported to have juvenile baldness[55], *Itgb6* KO animals largely recovered their normal hair coat in adult (Extended Data Fig. 10a). By 9 months, *Itgb6* KO did not show any defects in hair growth or in the bulge (Extended Data Fig. 10b). Similarly, *Cd34* and *Npnt* have also been individually deleted without affecting the maintenance of HF-SCs or displaying premature ageing phenotypes[28,56]. Thus, we concluded that genetic deletion of individual cell adhesion and ECM genes may not be sufficient to recapitulate HF ageing.

Collectively, our data provide evidence for a new model of SC exhaustion and HF miniaturization - dKO and aged HF-SCs fail to maintain the expression of many HF-SC-specific cell adhesion and ECM genes, at least in part as a result of reduced *Foxc1* and *Nfatc1* expression. In turn, the compromised niche and reduced cell adhesion allow epithelial cells to escape from the HF-SC compartment into the dermis, resulting in SC exhaustion and the eventual degeneration of HFs (Fig. 7g).

Discussion

Stem cell escape as a mechanism of cell loss and ageing

In this study, we have imaged HF-SC activities during ageing and in a *Foxc1/Nfatc1* dKO model in live animals. Leveraging the ability to noninvasively monitor HF-SC compartment at the time scale ranging from hours to weeks, we observed a hitherto unreported activity of epithelial cells escaping to the dermis. Although many of these escaping cells in both ageing and dKO mice are from the bulge region, it is possible not all escaped cells are stem cells. During ageing, the process of cell escape is relatively slow, and we could only monitor cellular activities of single HFs at the resolution of days. We have documented the disintegration of HFs accompanying by shedding epithelial cells to the dermis (Fig. 1f–g). In dKO, cell adhesion and ECM gene expression was strongly compromised, and this was correlated with more rapid epithelial cell escape and accelerated HF miniaturization. We have captured the process of HF-SCs migrating away from the epithelial niche and into the dermis in the time span of a few hours (movies S6–9). Although we were unable to label the BM, the most parsimonious explanation to the profound changes of nuclear shape and the distance these escaping cells traveled during the escape (movie S6) is that these epithelial cells squeeze through a small orifice of the defective BM and migrate into the dermis. These striking results provide the first direct evidence, to the best of our knowledge, that live epithelial cells transverse the BM and reach the dermis. These unexpected observations raise a number of questions for future investigation such as how these epithelial cells remodel cell

adhesion and detach from each other, gain the motility, and change their shape during the escape.

We were unable to identify a single cell adhesion or ECM gene, whose loss recapitulates cell escape or premature ageing phenotype. This is perhaps not surprising because ageing and tissue deterioration are generally caused by functional decline of many rather than singular contributing factors[1,2]. Indeed, altered HF-SC microenvironment has also been shown to drive HF ageing[6]. Thus, HF ageing is likely controlled by many different regulators. Interestingly, deletion of E-Cadherin in the HF-SC compartment causes HF-SC proliferation without triggering HF-SC depletion or premature ageing[57]. Furthermore, the increased HF-SC proliferation is caused by the loss of E-Cadherin in the inner bulge niche layer but not by the defects on the BM of the outer bulge[7,57]. Thus, the mechanism underlying the cell escape and subsequent SC depletion is distinct from the defective adherens junction. Finally, this new mechanism mediated by epithelial cell escape likely functions in parallel to well-studied cell exhaustion mechanisms such as cell death and senescence, and adds a new layer of biology to tissue degeneration.

Homeless epithelial cells in aged skin

With live imaging, we have uncovered the presence of escaped, homeless epithelial cells in the dermis of aged and dKO skin. Judging by their label by the *Krt14-H2bGFP* transgene and their rapid escape through the BM, it is likely that these cells do not undergo profound cell fate change such as epithelial-to-mesenchymal transition prior to their escape. These epithelial cells also persist in the dermis rather than immediately initiating programmed cell death such as anoikis upon the escape (Fig. 1f–g and movie S9). These observations raise important questions such as whether these escaped cells can self-renew or divide in the dermis, how do they interact with the foreign environment including dermal fibroblast cells, adipocytes and immune cells, and whether these escaped cells play any role in tumorigenesis during ageing. These questions warrant future investigation for the fate of escaped cells in normal and pathological conditions.

Mechanisms governing stem cell quiescence and the niche

Our data suggest that HF-SC quiescence and their niche integrity are coupled through the function of *Foxc1* and *Nfatc1.* Our previous study suggests that HF-SC activation promotes the expression of *Foxc1*, and in turn *Foxc1* reinforces quiescence by inducing *Nfatc1* and Bmp expression in activated HF-SCs[10]. Furthermore, *Foxc1*-mediated HF-SC depletion has been linked to defective adherens junctions although deletion of E-Cadherin does not cause HF-SC depletion or premature ageing[7,57]. Now by examining the transcriptome that are controlled by *Foxc1* and *Nfatc1*, we find that these two TFs co-regulate a large number of HF-SC specific cell adhesion and ECM genes, including *Cd34, Npnt* and *Itgb6.* Importantly, we show that the lack of HF-SC division in prolonged telogen during ageing also reduces *Foxc1* and, to a less extent, *Nfatc1* expression. Thus, HF-SC division may serve as a mechanism to rejuvenate cell adhesion of HF-SCs through the upregulation of *Foxc1.*

Our study has further revealed that the loss of SC quiescence *per se* does not directly cause SC exhaustion. Indeed, increased HF-SC proliferation does not deplete HF-SCs[57].

Furthermore, we observed numerous rapidly growing HFs when macroscopic hair loss was already widespread (Fig. 4g). Instead, dKO HF-SCs downregulated cell adhesion and ECM genes and escaped from the defective niche, resulting in excessive cell loss and hair degeneration. In support of this view, we still observed cell division and escape events concurrently in miniaturized HFs (movie S7). This model of SC exhaustion provides a new framework for studying SC quiescence and the integrity of SC niche.

Methods

Mice

All experiments are carried out by following IACUC approved protocols and guidelines at CU Boulder and Northwestern, respectively. Mice were bred and housed according to the guidelines of IACUC at pathogen-free facility at the University of Colorado at Boulder (CO, USA) and at Northwestern University Feinberg School of Medicine (IL, USA). The following mouse lines were used: K14Cre (E. Fuchs, Rockefeller University), K14-H2BGFP (E. Fuchs, Rockefeller University), Foxc1fl/fl, Foxc1-LacZ, Nfatc1fl/fl, Itgb6$^{-/-}$ (D. Sheppard, University of Californica, San Francisco), K15CrePR (Jackson lab, #005249) and Rosa26-LSL- tdTomato (Jackson lab, #021876).

K15CrePR induction was performed by topical application of 4% RU486 (dissolved in ethanol) from P22 to P28 for seven consecutive days. The samples were collected two or three days later at P30 or P31. Gender and age matched mice were used for FACS and histology. For quantification, at least 30 hair follicles from at least 3 pairs of animals were counted. Male and female mice show similar phenotypes, and the final results were reported by combining all data.

Horizontal whole mount staining

Back skins were embedded in Optimum Cutting Temperature (OCT, Tissue-Tek®) compound. Sections (100 μm) were prepared and incubated in PBS to remove the OCT. Horizontal whole mount staining was performed as previously described[1] with minor modifications. Briefly, Sections were fixed in 4% PFA for 10 minutes at room temperature, blocked in 0.5% Triton X-100, 0.25% fish skin gelatin, 0.5% skim milk powder in PBS (blocking solution) for 1 hour at room temperature and incubated overnight in primary antibodies at 4°C. Antibodies were diluted in blocking solution. After incubation, the sections were washed three times in 1xPBS for 2–3 hours. Secondary antibodies were added at a dilution of 1:1000 together with 5 μg/ml Hoechst33342 (Invitrogen) for 1 hour at room temperature, followed by washing three times in 1xPBS for 30 minutes. Sections were then placed on slides in VECTASHIELD® antifade mounting media (Vector Laboratories, H-1000) under a dissection microscope to ensure correct orientation, and then covered by coverslips for imaging. Confocal imaging of whole mount staining was performed on a Nikon A1 lase-scanning confocal microscope with either 20× 0.75 NA or 100× 1.49 NA objective lens and acquired with NLS Elements (Nikon) software in the University of Colorado, Boulder, Light Microscopy Core Facility.

Cryo-section and immunostaining

OCT embedded tissues were sectioned to 20–30 μm and fixed with 4% PFA for 10 min at room temperature. Sections were permeabilized for 10 min at room temperature with 0.1% Triton X-100 in 1× PBS. When staining with mouse monoclonal antibodies, we used the mouse-on-mouse basic kit (BMK-2202; Vector Laboratories). Otherwise, blocking was performed in 5% normal serum of the same species the secondary antibody was raised in. Sections were incubated with primary antibody overnight at 4°C. After incubation with primary antibodies, sections were washed three times in 1× PBS and incubated for 1 h at room temperature with Alexa Fluor 594–, Alexa Fluor 488–, or Alexa Fluor 647–conjugated secondary antibodies (1:2,000; Invitrogen/Molecular Probes). Nuclei were stained with Hoechst 33342 (1:5,000; Invitrogen).

Fluorescence-activated cell sorting

Gender and hair cycle matched mice were euthanized and collected for dissection. We first shave the hair coat and apply nair hair removal lotion (Amazon, 22339) for around 3 minutes. After wiping off the lotion and washing away leftover hair shaft, back skin was dissected and subcutaneous fat was removed using a blade. Small part of the skin sample was embedded in OCT and the remaining skin sample was minced and incubated with 0.25% collagenase (Worthington, LS004188) in 4–6mL 1x HBSS buffer at 37°C for 2 hours with rotation. 5mL serological pipet was used to further separate epidermis from dermis at 1hour incubation time. After collagen treatment, we added 10mL cold PBS and centrifugated the sample at 400g for 10minutes at 4°C. The pellet was resuspended with pre-warmed 0.25% trypsin/EDTA(Gibco) for 8minutes at 37°C and the digestion was immediately blocked by adding 10mL cold 1xPBS with 3% chelated FBS. The suspension was extensively triturated with a 10ml pipette and passed over a 40um cell strainer, followed by centrifugation at 400g for 5 minutes at 4°C. The pelleted cells were resuspended in cold 1xPBS with 3% chelated FBS. Cells were incubated with appropriated antibodies for 1 hour on ice. DAPI was used to exclude dead cells. Hair follicle stem cells (HF-SCs) of K14Cre- based experiments were isolated by enriching $DAPI^{neg}$, K14-$H2BGFP^{hi}$, $Sca1^{lo}$, $\alpha6^{hi}$ and $CD34^{hi}$ cells. HF-SCs of K15CrePR- based experiments were isolated by enriching $DAPI^{neg}$, K14-$H2BGFP^{hi}$, $tdtomato^{hi}$, $Sca1^{lo}$ and $CD34^{hi}$ cells. The following antibodies were used: integrin α6 (CD49f, 1:75; eBioscience, PE-conjugated, 12–0495; APC-conjugated, 17–0495), CD34 (1:50; eBioscience, eFluor 660-conjugated, 50–0341), Sca1 (Ly-6A/E, 1:500; eBiosciences, PerCP-Cy5.5-conjugated, 45–5981). FACS was performed on MoFlo XDP machine (Beckman Coulter). FACS data were analyzed with FlowJo.

RNA-seq assay

Total RNAs from FACS-purified cells were isolated using TRIZOL(Invitrogen) and RNA quality was assessed by Agilent 2100 bioanalyzer. RNAs with integrity numbers (RIN)>8 were used to perform RNA-seq assay. Libraries were prepared following manufacturer's protocol (NEBNext Ultra Directional RNA Library Prep Kit). The cDNA libraries were quality-checked with bioanalyzer before sent out for sequencing at Genomics and Microarray Core Facility at University of Colorado Denver on Illumina NovaSeq 6000.

Omni-ATAC-seq assay

Assay for transposase accessible chromatin followed by sequencing (ATAC-seq) was performed as previously described[2] with modifications: An average of 50,000 FACS-sorted HF-SCs were collected in PBS containing 3% chelated fetal bovine serum (FBS) and pelleted by centrifugation for 5min at 500g at 4°C. Cell pellets were resuspended in 50ul of lysis buffer containing(10mM Tris-HCl pH 7.4, 10mM NaCl, 3mM MgCl2, 0.1% Igepal CA-630, 0.1% Tween-20, 0.01% Digitonin) and incubated on ice for 3 minutes. After the incubation, we added 1mL of wash buffer containing 10mM Tris-HCl pH 7.4, 10mM NaCl, 3mM MgCl2, 0.1% Tween-20 and inverted the tube 3 times to mix. The nuclei were then pelleted by centrifugation for 15min at 500g, 4°C. Supernatant was carefully discarded and nuclei were resuspended in 50 ul reaction buffer containing 5ul of Tn5 transposase and 25ul of TD buffer (Nextera DNA Sample Preparation Kit, Illumina), 16.5ul PBS, 0.5ul 1% Digitonin, 0.5ul 10% Tween-20 and 5ul H2O. The reaction was incubated at 37°C for 30min with rotation, terminated by adding 10ul of clean-up buffer (900mM NaCl, 300mM EDTA) and immediately purified using MinElute PCR Purification Kit (QIAGEN). After the purification, the DNA samples were quantified using nanodrop and 50ng of DNA was used for library construction. Library amplification was performed for 13 cycles following the manufacturer's protocol (Nextera DNA Sample Preparation Kit, Illumina) except using 2.5ul of each primer and 2min of extension time in PCR reaction. Libraries were sized-selected to enrich 150–1000bp of insert size, quality-checked with bioanalyzer and sequenced as paired-end for at least 40 million reads per sample.

Single-cell ATAC assay

Cells from both wild type and dKO animals were collected from FACS sorting machine with cell surface proteins and H2BGFP signals such that epidermal cells and hair follicle cells are 1:3 ratio. 10k cells were used for both WT and dKO scATACseq preparation. The libraries were prepared using 10X Chromium Single Cell ATAC Library & Gel Bead Kit (PN-1000110). In brief, cell nuclei were isolated and nuclei suspension were incubated in a transposition mix to fragment the DNA and add adaptor sequence to the end of DNA fragments. Single nuclei resolution was achieved using 10X barcoded gel beads, partitioning oil, a master mix on a Chromium Chip E. The libraries were constructed using 10x sample index plate and double size selected between 150bp to 1000bp.

Intravital live imaging

Intravital live imaging was performed as previously described[3,4] with modifications. The mice used for imaging was sedated using 2% oxygen and ~1–2% isoflurane. Once the mouse was fully sedated (~5minutes), it was put on a warm pad at 37°C. The oxygen and isoflurane were maintained during the course of imaging. Night-time ointment (Genteal, NDC 0078–0473-97) was applied to keep the eyes moisturized. 30-gauge needle and tattoo ink were used to mark the region (best mark the region at least one day before imaging to allow for healing). Custom manufactured spatula was used to stretch and flatten the region of interest (near the tattoo ink) and maintained at adjustable height. The double sides tapes were used to adhere the lower side of ear onto the spatula. After applying long-lasting Genteal gel (0078–0429-47) to the region of interest, a second adjustable spatula, glued

with cover-glass on one end, was gently pressed down to the ear so that the cover glass is right on top of the region. The second round of long-lasting Genteal was applied on the cover-glass (the Genteal should cover large enough region for the objective to move around and large enough amount to keep the tip of objective merged in during imaging). We used the Olympus FVMPE-RS multiphoton imaging system for acquiring images. The laser we used were Insight X3 with wavelength set to 920nm for GFP signals and Maitai HP with wavelength set to 850nm for SHG signals. Emission wavelength were 510nm and 430nm respectively. We used 10X and 25X objectives for images. During the imaging session, the light should be turned off and the stages and scope should be covered with black curtain to avoid exposure to light. After the image session is done, the mouse was kept in oxygen for around 10 minutes to recover before sending back in cage.

Two-photon image processing and quantification

Two photon images were acquired using Fluoview software from Olympus. The images were opened up using fiji (imagej) and converted to tif format using fiji > plugins > bio-formats > bio-formats-exporter. The time lapse images were aligned using plugins > registration > descriptor-based series registration (2d/3d +t) before exported. The exported tif files were further converted to imaris file using imaris file converter. The Imaris x64 9.2.1 were used to open up file for further analysis. The images were adjusted on x, y or z plane and smoothen with Gaussian filter for better visualization. Movies were also adjusted and generated from Imaris. For hair follicle quantifications, the 3D pictures were opened in Imaris and then cut off the epidermis and upper hair follicle regions. The leftover bulge regions were applied with 3d rendering to model the surface area. The surface area output was used for quantification and plotting. For hair follicle miniaturization, we use the smallest hair follicle in young samples as cutoff, any hair follicle smaller than the cutoff was counted as miniaturized. To quantify the number of HF-SCs, we used the 3D 2-photon images to select one sagittal plane and count all the HF-SCs in the outer layer.

To quantify the HF fate, we tracked 78 total HFs for at least 16 days and monitor HF morphological changes. We defined Regeneration as HFs that are cycling and there are no signs of shrinkage while in telogen; Degeneration as noncycling HFs undergo miniaturization or cycling HFs getting smaller in telogen; Quiescence as noncycling HFs and no significant size change during tracking.

To quantify the immune-staining signals of Foxc1 and Nfatc1 in HFSCs, we co-stained with Cd34 to label the bulge region and HFSCs. The images were then converted to Imaris for further quantification. Briefly, we used Imaris Surface module to manually select a fixed-size circle in the nucleus in HF-SCs. The mean/median intensity of each channel of the selected region was obtained from the statistical tab.

RNA-seq analysis

RNA-seq reads (150nt, paired-end) were aligned to the mouse genome (NCBI37/mm10) using Hisat2 (version 2.1.0)[5]. The resulting sam files were converted to bam files using samtools (version 1.3.1)[6]. Expression measurement of each gene was calculated from the resulting alignment bam file by HT-seq[7]. Differentially expressed genes were determined

using DEseq2[8] with adjusted p-value cutoff of 0.05. Gene ontology analysis was performed using Metascape[9]. The selected GO terms were from the metascape results along with the genelists.

Single-cell RNA-seq analysis

The Cell Ranger Single-Cell Software Suite was used to perform barcode processing and single-cell 3' gene counting (http://software.10xgenomics.com/single-cell/overview/welcome). The barcodes, features and matrix files were loaded into Seurat 3.0[10] for downstream analysis (https://satijalab.org/seurat/vignettes.html). For each sample, the analysis pipeline followed the guided tutorial. The cells were filtered with nFeature_RNA (>200 and <5000) and mitochondrial percentage (< 10). In addition, the cell cycle regression was used to regress out addition variation from cell cycle genes. After clustering and umap dimension reduction, the cluster markers were used to identify distinct cell population. For comparison among different samples, all samples were integrated to promote the identification of common cell types and enable comparative analysis[11]. All the differential analyses were based on non-parameteric Wilcoxon rank sum test. The avg_logFC were converted to log2_FC for consistency with bulk RNAseq. Genes with lower than 0.05 adjusted p valued were used for GO term analysis.

To re-cluster specific cell populations, we first subset the cells of interest and then re-run the analysis pipeline with modifications on umap resolution.

For differential gene plot, we used both default Seurat options and scanpy[12]. Note that we used cell cycle regression for initial clustering of total populations, but for pseudotime analysis, we didn't regress out cell cycle genes in order to capture differentiation information. After clustering, we were able to resolve Lgr6+ HF-SC, we thus named upHFSC population. Then we kept only the HF lineages including HFSC, UpHF, INF, Niche, HG, UpHFSC and SG based on Seurat clustering. Then, we converted the Seurat object to single cell experiment for standard downstream monocle3 pseudotime analysis[13]. After getting the pseudotime score for each cell, we first filtered out all the cells without scores (which are mostly SG) and then added the information back to Seurat object for further plotting.

ATAC-seq and motif analysis

ATAC-seq reads (paired-end) were aligned to mouse genome (NCBI37/mm10) using Bowtie2 (version 2.2.3)[14]. Duplicate reads were removed by Picard tools (http://broadinstitute.github.io/picard/). Mitochondrial reads were removed and peaks were called on each individual sample by MACS (version 2.0.9)[15]. Peaks from different ATAC-seq samples were merged for downstream analysis. De novo motif discovery was performed using the HOMER[16]. Motif scanning was done by MEME (5.0.3)[17]. The bedfiles were converted to fasta file by bedtools getfasta[18], and motifs discovered by HOMER were used to scan for instances in open chromatin regions. The HOMER motifs were also converted to meme format by R package from github (https://gist.github.com/rtraborn/e395776b965398c54c4d). For IGV visualization[19], we first concatenate all the peaks from samples of interest and convert it into gtf file, count the number of reads mapped in peaks

and then normalize all samples using 'bedtools genomecov -scale' to get the bedgraph files. Igvtools toTDF was used to get tdf files for final visualization.

Single-cell ATAC-seq analysis

The fastq files were collected from sequence facility and concatenated together. We used cellranger-atac (version 3.0.1) count with reference downloaded from 10x genomics website. Loupe Cell Browser (version 3.1.0) were used to generate t-SNE plot of WT and dKO samples. We used graph-based clustering for p28 control samples and k-means based clustering for p28 dKO samples for better identification of subpopulations.

The IFE and HFSC populations were first extracted from the bam file of cell ranger atac output file. First, we extracted cluster ID of each population and used the suggested methods from 10xgenomics (https://kb.10xgenomics.com/hc/en-us/articles/360022448251-Is-there-way-to-filter-the-BAM-file-produced-by-10x-pipelines-with-a-list-of-barcodes-) to subset bam files specific for each population. To predict the cis-regulatory landscape from scATAC data, we used R package Cicero[20] to infer enhancer and promoter interaction. The pipeline was performed according to the tutorial. The cicero connection lists were exported from R and saved for further analysis. For connection score at transcriptional start sites (TSS), we first downloaded mouse gene coordinate gff file from UCSC genome browser, then we extract the gene TSS sites based on the gene coordinates and strand information. The cicero peaks were imported to python and use pandas to covert to bed file format. The formatted cicero bedfiles were used to intersect with TSS bedfile to extract the peaks connected to the TSS sites and corresponding connection scores. For each individual gene, the connection scores were first filtered with 0.2 as cutoff and then all the connections were summed up as total score. For the global reduced enhancer-promoter interactions, we first used all the connection scores greater and equal than 0.16 to reduce noise, then organized and formatted all of the peaks from control and dKO samples for comparison. We considered any interactions with greater or equal to 0.2 as changed interactions, and less or equal to 0.1 as background interactions. All of the peaks with corresponding interactions were pooled, filtered out the peaks with transcription start sites, and then used HOMER[16] for *de novo* motif discovery.

K-Means Clustering of ATAC Peaks

To compare open chromatin signals across multiple samples, K-means Clustering was performed using seqMINER (version 1.3.4)[21]. The bamfiles were firstly converted to bedfile using bedtools bamtobed. To normalize across samples for depth of sequencing we downsampled each bedfile to 20M reads for input. Peaks were called by MACS2 from all the bulk ATACseq data. Then the peaks called from bulk data were concatenated, sorted, merged and then used as genome coordinate. Signals were calculated in a 1.5kb region (±750 bp) surrounding the center of the peak with 50 nt bin.

Statistics and study design

In general, all sequencing experiments (RNA-seq, ATAC-seq) were repeated on at least two pairs of control and cKO/dKO samples per experiment. Single-cell ATAC-seq was performed with one pair of control and dKO samples at the same time on the same chip to

avoid the batch effect. All experiments were designed such that there were always littermate controls. All statistical tests performed are as indicated in the figure legends. No statistical methods were used to predetermine sample size. The experiments were not randomized and the investigators were not blinded to allocation during experiments and outcome assessment, except where stated.

Statistics and Reproducibility

Results in Fig1a,b,f-i, are repeated in at least three different animals. Results in Fig4a, j are repeated in at least three different animals. Results in Fig5h. are repeated in at least three different animals. Results in Fig7a,b,d, e, f are repeated in at least three different animals. Results in Fig7c are observed in 2 different animals. Results in Extended Data Fig. 1a,b,d,h; 4a–c; 5b, e, g, i; 7a and 10b are repeated in at least three animals.

Extended Data

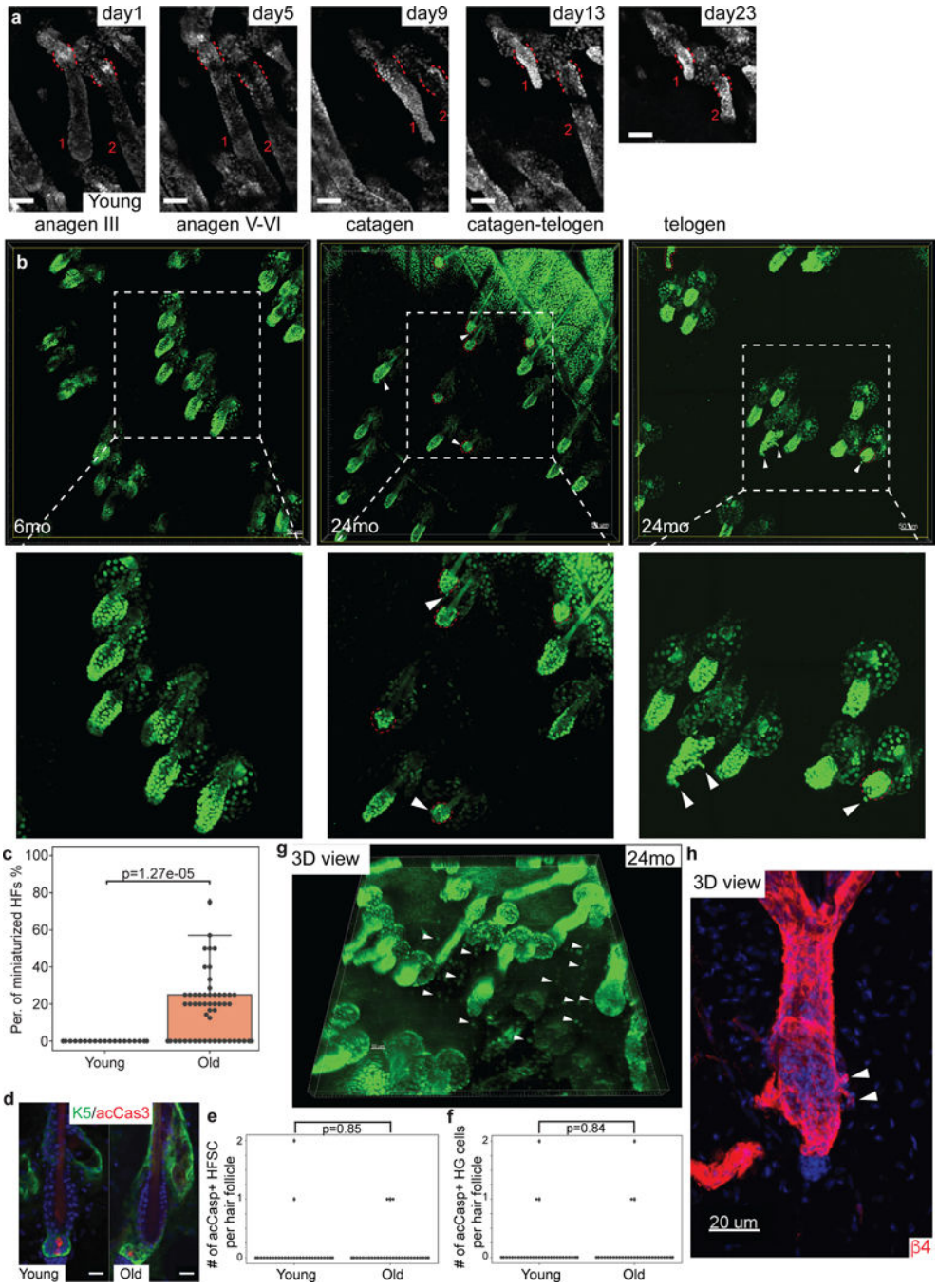

Extended Data Fig. 1. Live imaging of escaped cells in aging hair follicles.

a, Two-photon longitudinal tracking of hair follicles in young mice during the anagen to telogen hair cycle. Red numbers designate the same hair follicle in each image. Red dotted lines annotate the bulge region. Scale bar, 50μm. **b**, Two-photon intravital imaging of hair follicles from young (left panel) and old (middle and right panels) mice. White arrowheads point to miniaturized hair follicles and cells located outside of the HF-SC compartments.

Red dotted lines outline miniaturized hair follicles. Scale bar, 50μm. **c**, Boxplot of the percentage of miniaturized hair follicles, quantified from 3-D scan of live animals. (n=205 HFs from 5 young mice; n=327 HFs from 3 old mice). **d**, Representative images of hair follicles with KRT5 and activated caspase 3 (acCas3) signals in young (6~8mo) and old (20mo) mice. (n=50 hair follicles from young mice; n=62 hair follicles from old mice, 3 pairs of mice). Scale bar, 20μm. **e-f**, Boxplot of number of acCas3+ HFSCs(e) and HG(f) per hair follicle (n=50 hair follicles from young mice; n=62 hair follicles from old mice, 3 pairs of mice). **g,** 3-D view of hair follicles in 24mo old mice. White arrowheads point to numerous escaped epithelial cells scattering in the dermis. Scale bar, 50μm. **h,** 3-D view of β4 integrin immunofluorescence signals in 24mo old mice. White arrowheads point to HF-SCs with protruding integrin signals in the new bulge side. Scale bar, 20μm.

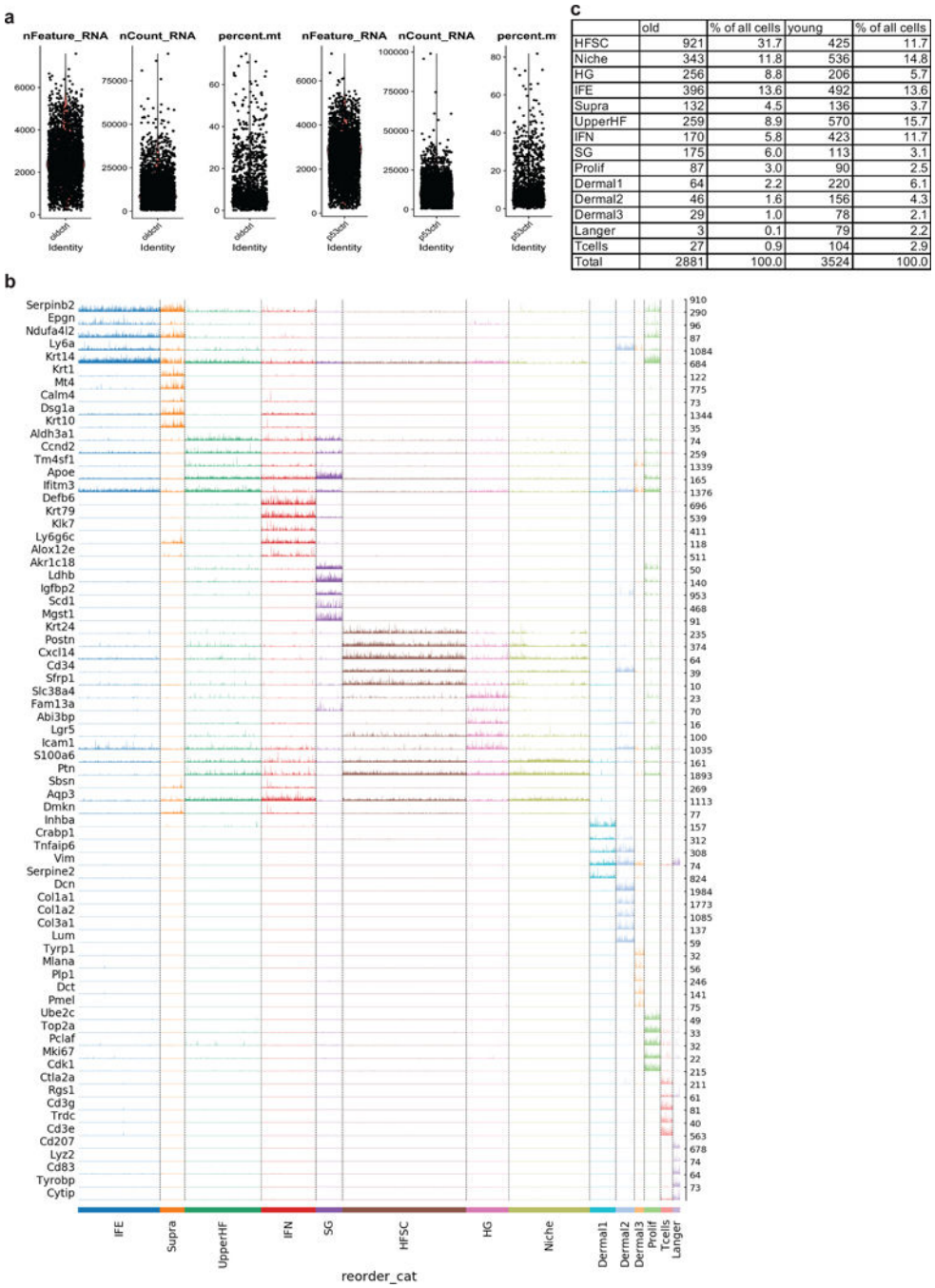

c

	old	% of all cells	young	% of all cells
HFSC	921	31.7	425	11.7
Niche	343	11.8	536	14.8
HG	256	8.8	206	5.7
IFE	396	13.6	492	13.6
Supra	132	4.5	136	3.7
UpperHF	259	8.9	570	15.7
IFN	170	5.8	423	11.7
SG	175	6.0	113	3.1
Prolif	87	3.0	90	2.5
Dermal1	64	2.2	220	6.1
Dermal2	46	1.6	156	4.3
Dermal3	29	1.0	78	2.1
Langer	3	0.1	79	2.2
Tcells	27	0.9	104	2.9
Total	2881	100.0	3524	100.0

Extended Data Fig. 2. Quality control and clustering of single-cell RNA-seq data from young and old mice.

a, Quality control and filtering of single cells from old and young samples. Cells were filtered with detected genes numbers (200<nFeature_RNA<5000), transcripts numbers (nCount_RNA) and mitochondrial percentage (percent.mt < 10). **b**, Track plot of marker genes for each cluster. **c**, Table shows cluster names, cell numbers and percentage of cells for each cluster after filtering of old and young scRNA-seq data.

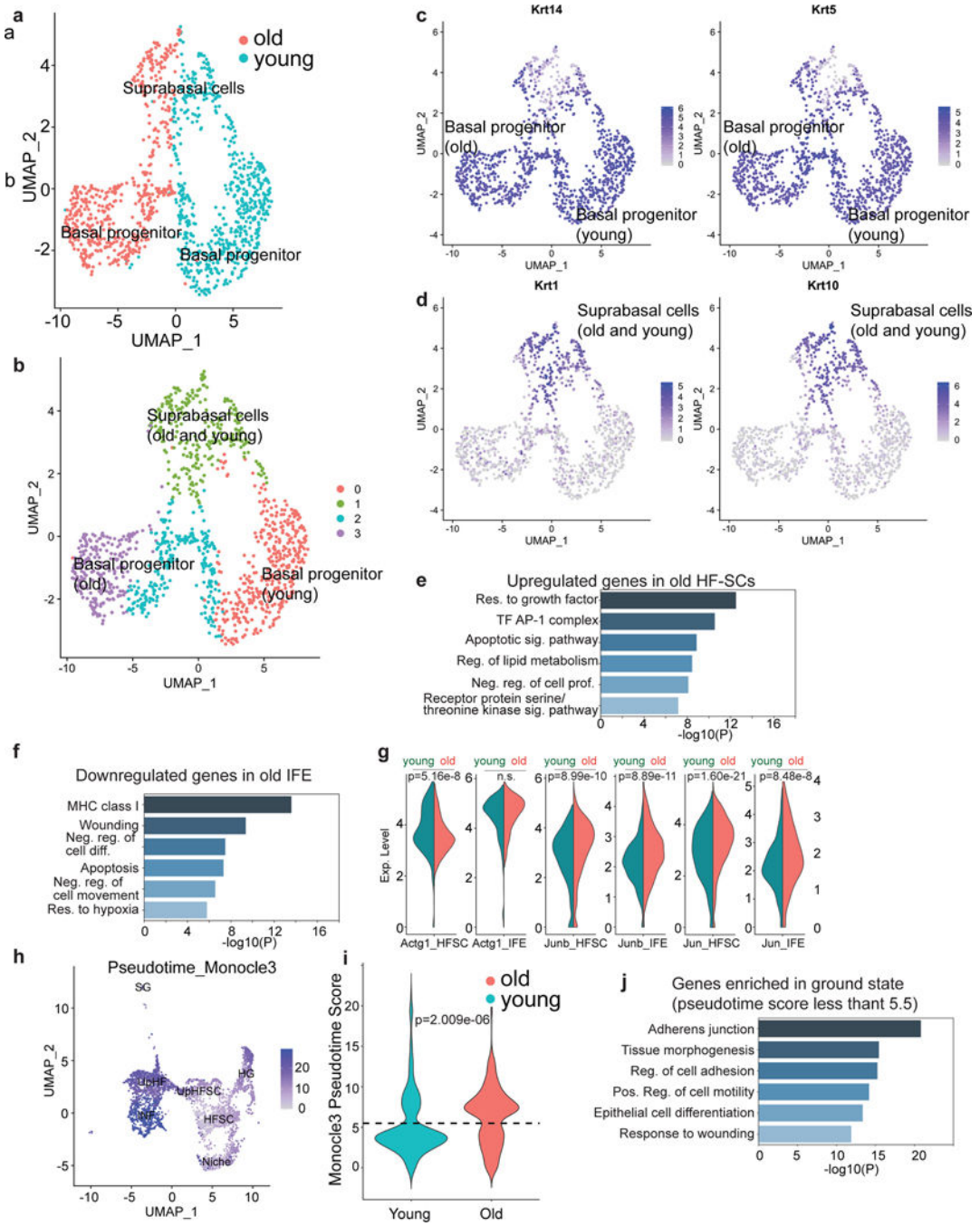

Extended Data Fig. 3. Single-cell transcriptomic analysis of old and young skin samples.

a-b, UMAP re-clustering and projection of IFE cells, color coded by sample identity (**a**) and cluster identity (**b**). **c-d,** Feature plots of marker genes for basal progenitor cells (Krt14, Krt5) and suprabasal cells (Krt1, Krt10). **e-f**, Highly enriched GO terms for upregulated genes in old HFSCs (**e**) and downregulated genes in old IFE (**f**). **g**, Violin plots of selected gens in young and old HF-SC and IFE cell clusters. **h**, Feature plot of monocle3 pseudotime score of hair follicle cells from old and young mice**. i**, Violin plot of HFSCs pseudotime

score in young and old samples. **j**, Highly enriched GO terms for HFSCs in the ground state with lower pseudotime score (<5.5).

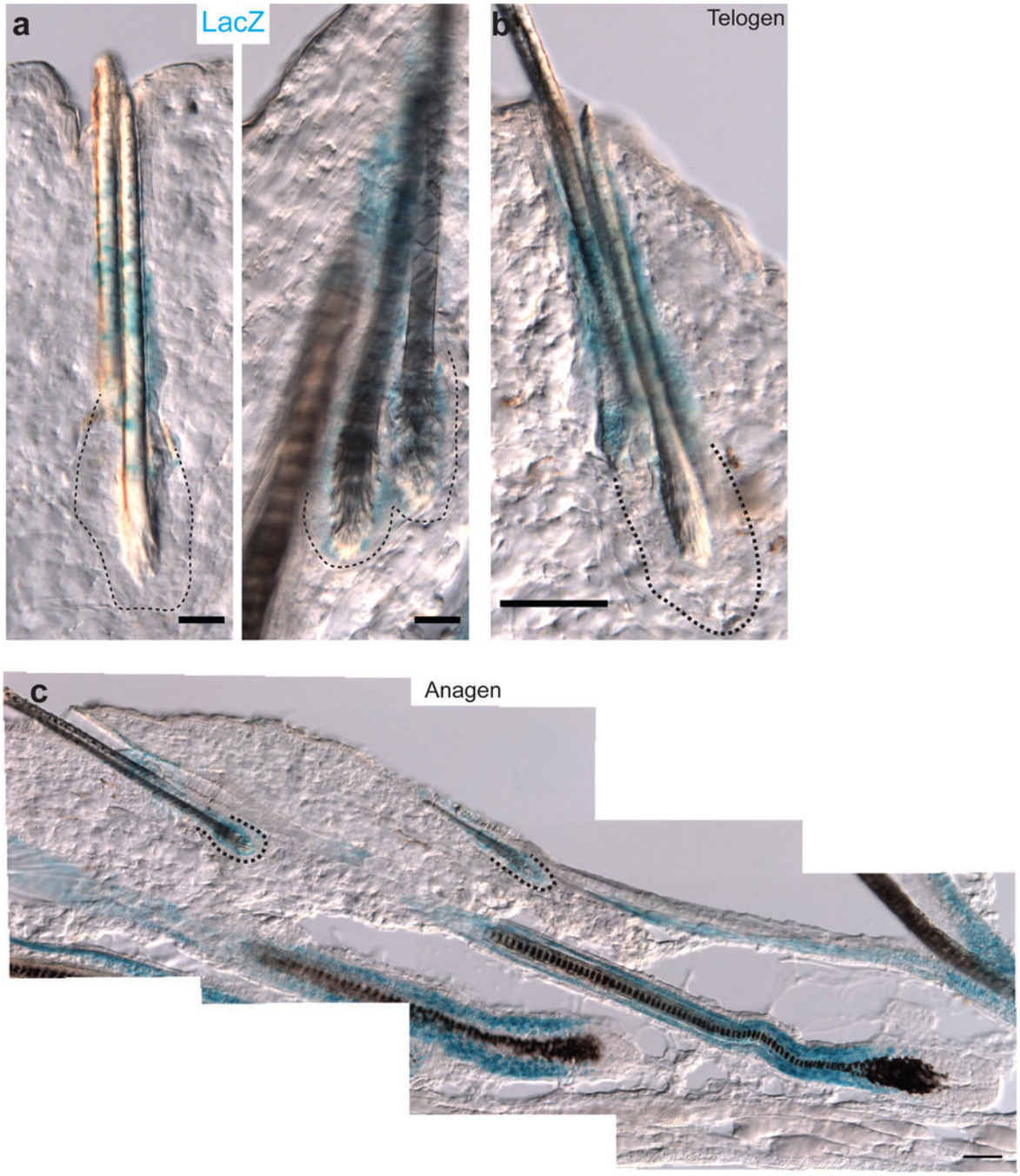

Extended Data Fig. 4. Transcriptional activity of *Foxc1* locus in 15mo old mouse skin.

a, Transcriptional activity of *Foxc1* locus (*Foxc1-LacZ* knockin) is detected in anagen bulge but not detected in telogen bulge. Scale bar, 20μm. **b**, Transcriptional activity of *Foxc1* locus (*Foxc1-LacZ* knockin) is not detected in telogen bulge. Scale bar, 20μm. **c,** Robust

transcriptional activity of *Foxc1* locus (*Foxc1-LacZ* knockin) is detected in both bulge and IRS regions of anagen hair follicles. Scale bar, 20μm.

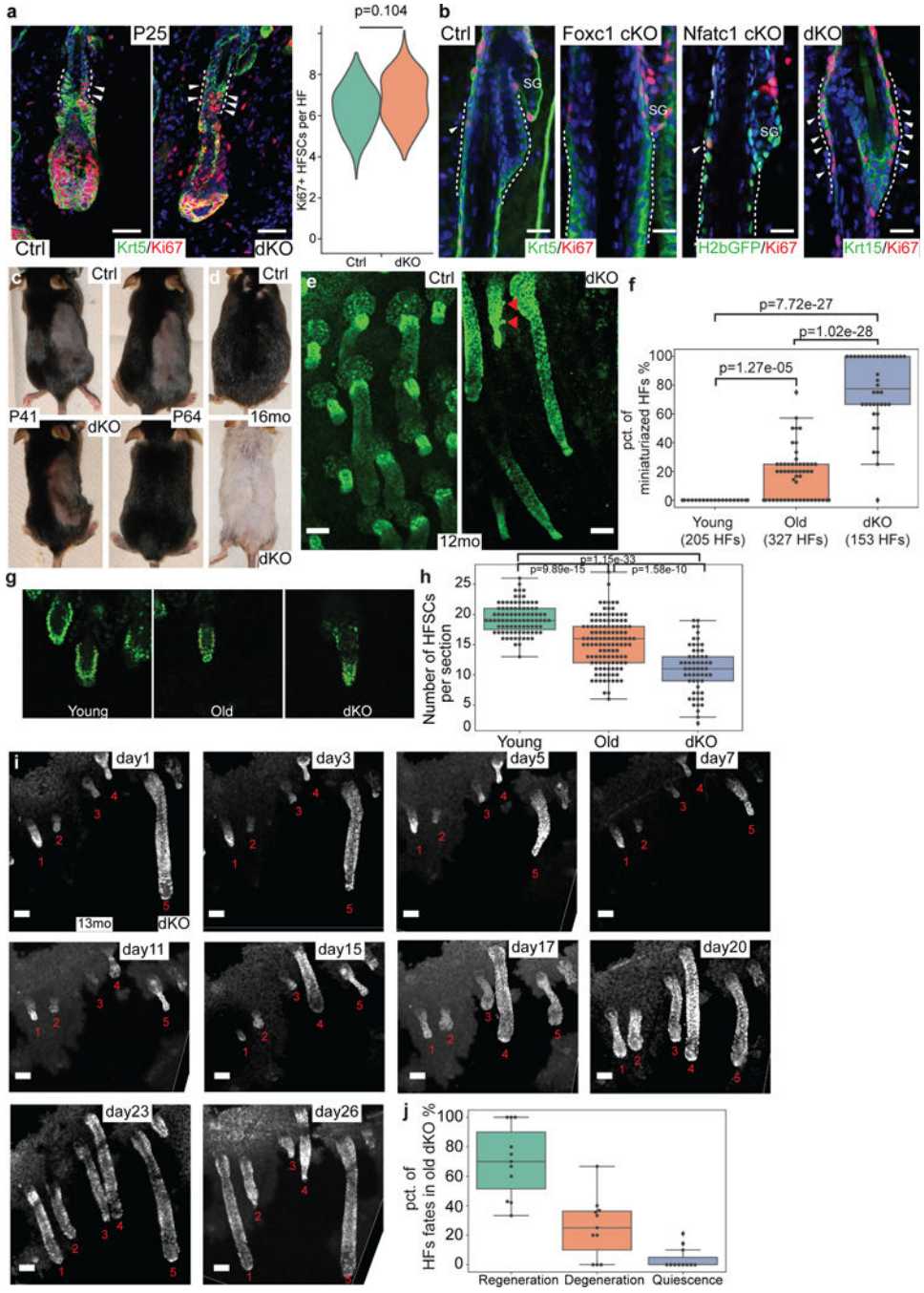

Extended Data Fig. 5. Hair follicle miniaturization and loss in dKO mice.

a, Krt5 and Ki67 staining of hair follicles at early anagen (anagen III, P25) in control and dKO mice, arrowheads indicate Ki67+ HF-SCs, Right panel, quantification of Ki67+ HF-SCs per hair follicle (n=30 hair follicles from 3 pairs of mice). Scale bar, 20μm. **b**, Ki67 staining of hair follicles at late anagen (anagen V-VI) in control, *Foxc1* cKO, *Nfatc1* cKO,

and dKO mice, arrowheads indicate Ki67+ HF-SCs. Scale bar, 20μm. **c**, Images of hair coat in the same control and dKO mice on P41 (left panel) and P64 (right panel), the right half of back skin was shaved on P41 and imaged again on P64. **d**, Images of hair coat of control and dKO mice at ~16mo old. **e**, Two-photon images of hair follicles in control and dKO mice at 12mo old, red arrowheads point to escaped cells outside of hair follicles. Scale bar, 70μm. **f**, Boxplot of the percentage of miniaturized hair follicles in young, old and dKO mice. (5 young mice; 3 old mice; 5 dKO mice). **g**, Representative Two-Photon images for the quantification of HFSCs, red asterisks mark HFSCs(g). **h**, Boxplot of the number of HFSCs per HF in different samples. **i**, Longitudinal tracking of dKO hair follicles over 26 days. Red numbers indicate the identical hair follicles in each image. Scale bar, 70μm. **j**, Boxplot of the percentage of HFs undergo regeneration, degeneration and quiescence in dKO samples (78 HFs from more than 3 mice were tracked for at least 16 days).

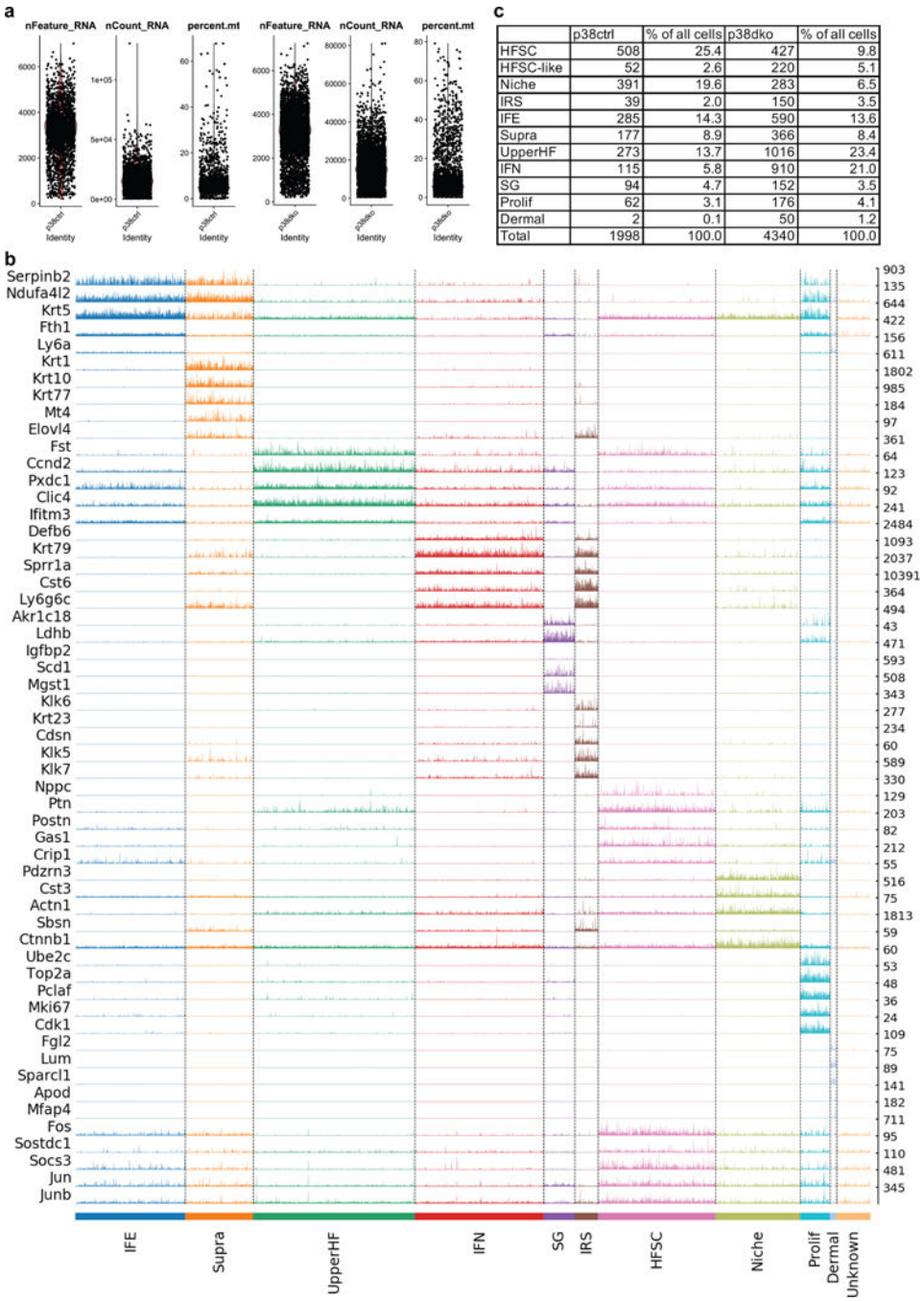

c

	p38ctrl	% of all cells	p38dko	% of all cells
HFSC	508	25.4	427	9.8
HFSC-like	52	2.6	220	5.1
Niche	391	19.6	283	6.5
IRS	39	2.0	150	3.5
IFE	285	14.3	590	13.6
Supra	177	8.9	366	8.4
UpperHF	273	13.7	1016	23.4
IFN	115	5.8	910	21.0
SG	94	4.7	152	3.5
Prolif	62	3.1	176	4.1
Dermal	2	0.1	50	1.2
Total	1998	100.0	4340	100.0

Extended Data Fig. 6. Quality control and clustering of single-cell RNA-seq data from control and dKO.

a, Quality control and filtering of single cells from both control and dKO samples at P38. Cells were filtered with detected genes numbers (200<nFeature_RNA<5000), transcripts numbers (nCount_RNA) and mitochondrial percentage (percent.mt < 10). **b**, Track plot of marker genes for each cluster. **c,** Table shows cluster names, cell numbers and percentage of cells for each cluster after filtering of both control and dKO single-cell RNA-seq data.

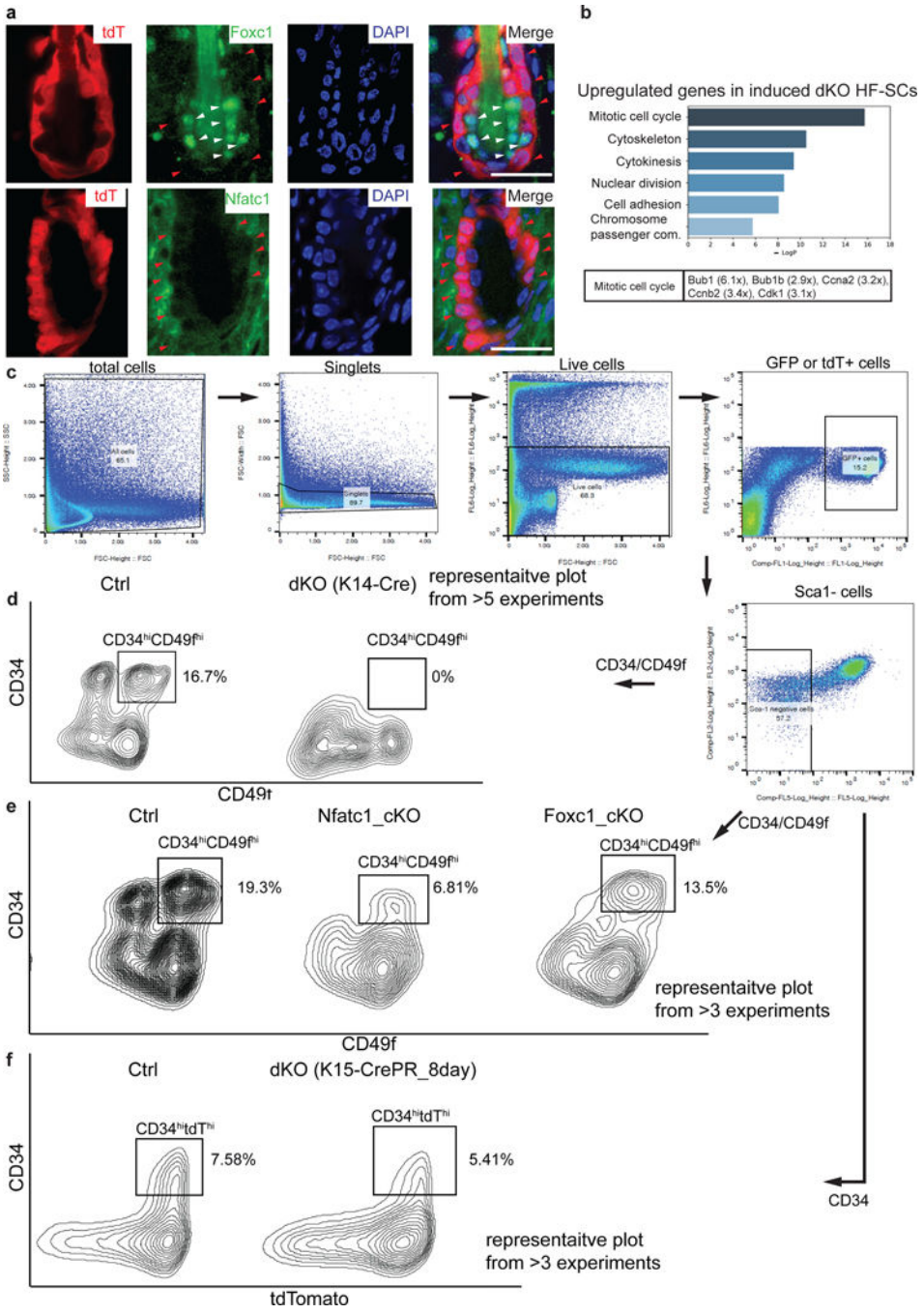

Extended Data Fig. 7. Isolation and transcriptomic analysis of *Foxc1* and *Nfatc1* single KO and induced dKO HF-SCs.

a, Immunofluorescence staining of *Foxc1* and *Nfatc1* in *Krt15-CrePR* induced dKO hair follicles. tdT is tdTomato signals from *ROSA26-LSL-tdT* allele, indicating Cre+ dKO HF-SCs. Red arrowheads indicate HFSCs without *Foxc1* and *Nfatc1* signals, white arrowheads indicate inner bulge region, which is negative for tdT. Scale bar, 20μm. **b**, Highly enriched GO terms of upregulated genes and selected differentially expressed in induced dKO HF-SCs. **c-d**, Flow cytometry analysis and quantification of HF-SCs during the first anagen

(P28-P31) in control, Krt14-Cre-mediated dKO hair follicles (**c**), *Foxc1* cKO and *Nfatc1* cKO hair follicles (**d**). The rectangle regions are CD34-APC^{hi} and Cd49f-PE ^{hi} HF-SC populations. Representative plots for 3~5 sets of experiments are shown. **e**, Flow cytometry analysis of Krt15-CrePR-mediated dKO hair follicles with *ROSA26-LSL-tdT* allele to mark Cre+ dKO cells. The rectangle regions are CD34-APC^{hi} and tdTomato^{hi} populations. Representative plots for 5 sets of experiments are shown.

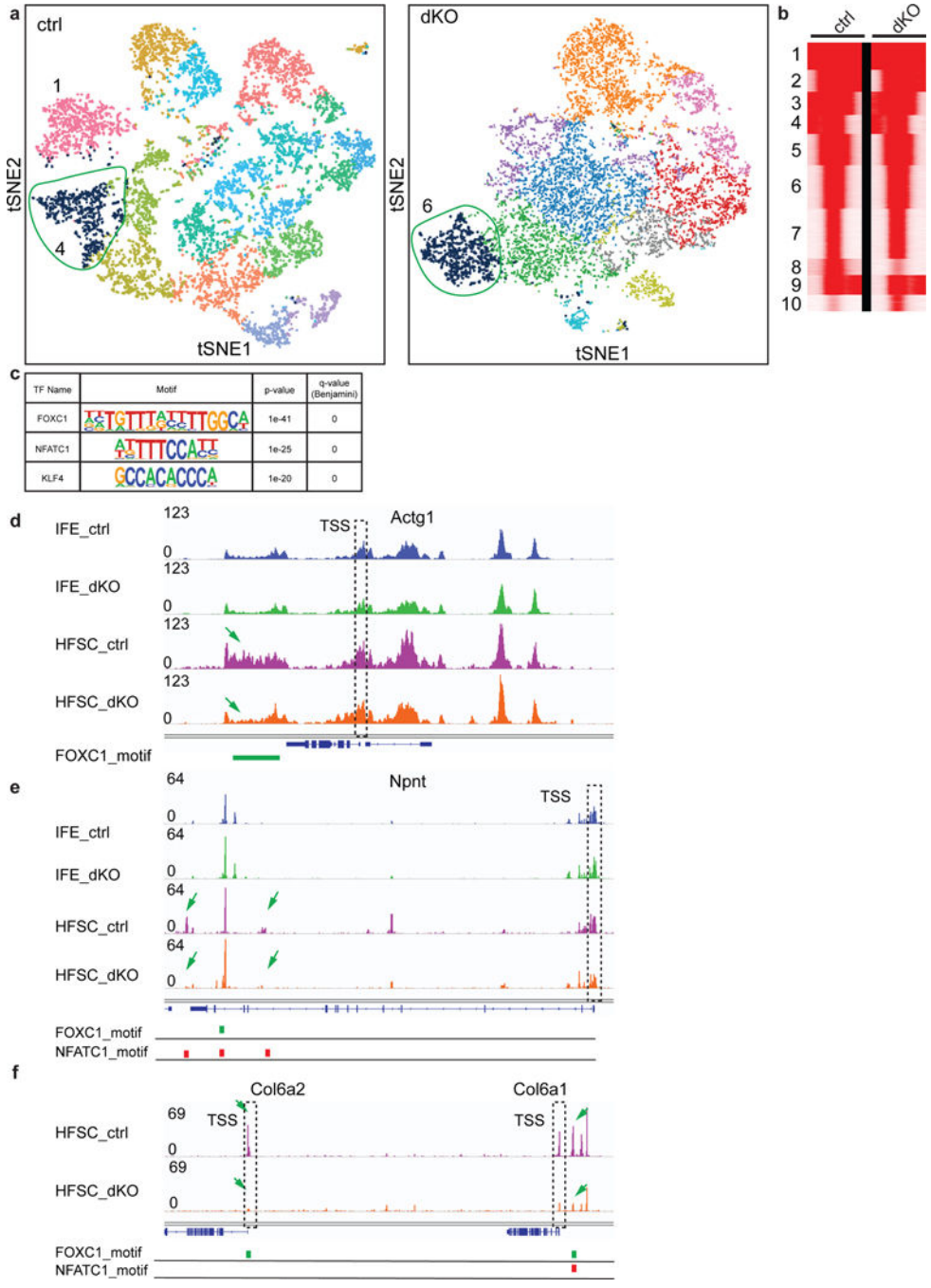

Extended Data Fig. 8. Single-cell ATAC analysis of *Foxc1* and *Nfatc1* controlled open chromatin in HF-SCs.

a, tSNE plots of control and dKO total epithelial cells (Krt14-H2bGFP+). The HF-SC populations in each sample are highlighted in blue color and circled. The selected populations show the strongest open chromatin signatures of *Cd34,* the marker for HF-SC, and the weakest signatures of *Gata6*, a differentiation marker. **b**, K-means clustering of control and dKO open chromatin regions from aggregated scATAC-seq data from the HF-SC populations. Cluster 8 is reduced in dKO and cluster 10 is enhanced in dKO. **c**, Top 3 most highly enriched transcription factor motifs in cluster 8. **d-f,** Aggregated scATAC-seq tracks of *Actg1* (**d**), *Npnt* (**e**) and *Col6a1/2* (**f**) loci annotated with FOXC1 and NFATC1 motifs. Location of FOXC1 (green marks) and NFATC1 (red marks) motifs are indicated. Arrows point to HF-SC-specific open chromatin regions that are lost in dKO and the dashed rectangles mark the TSS of *Actg1, Npnt* and *Col6a1/2,* respectively.

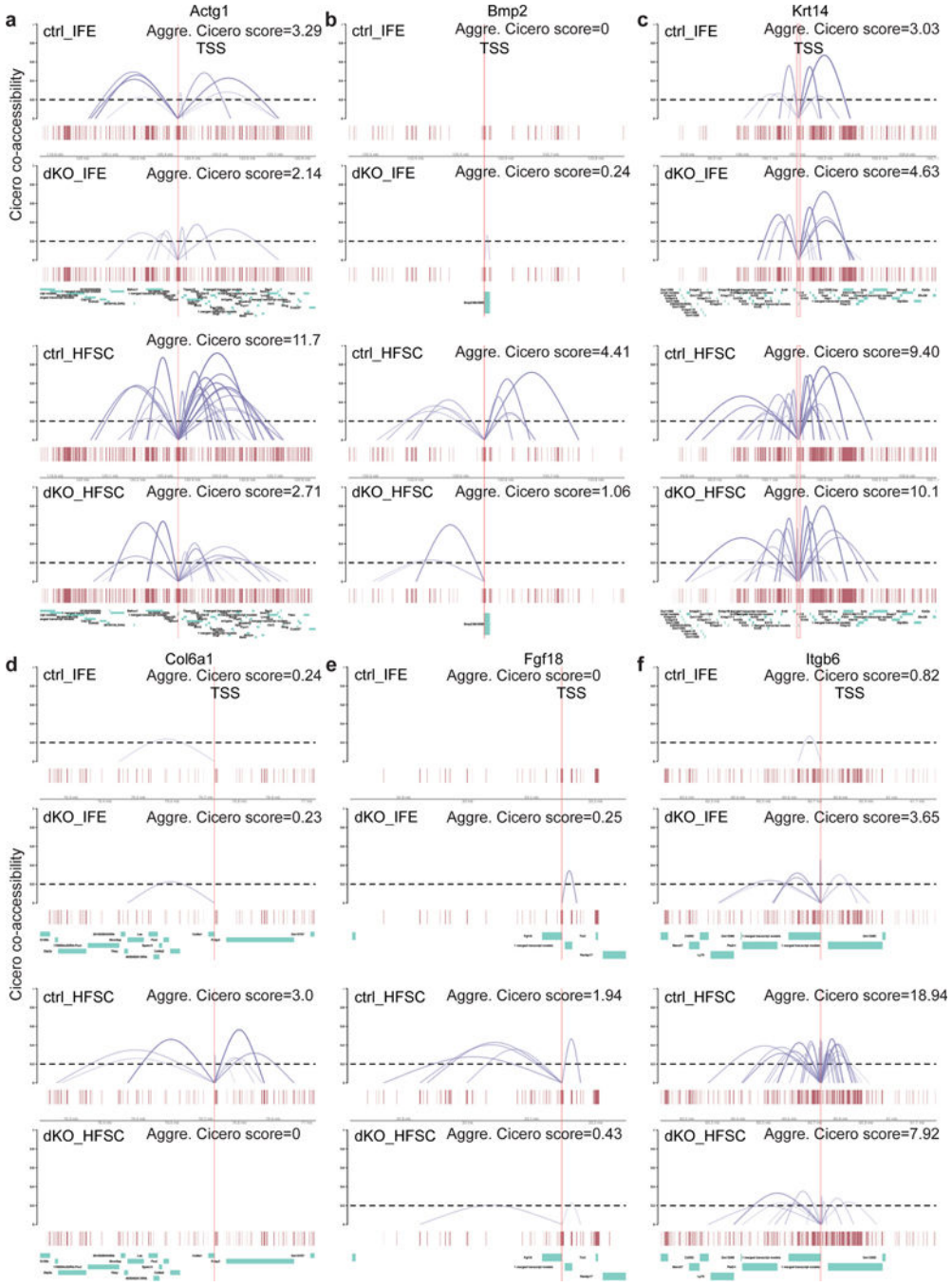

Extended Data Fig. 9. Enhancer-promoter interactions are inferred by using aggregated Cicero scores computed from scATAC-seq.

a-f, Enhancer-promoter interactions of *Actg1* (**a**), *Bmp2* (**b**), *Krt14* (**c**), *Col6a1* (**d**), *Fgf18* (**e**) and *Itgb6* (**f**) are illustrated in ctrl IFE, dKO IFE, ctrl HF-SC and dKO HF-SC. The aggregated Cicero score is calculated by the summation of Cicero scores of all enhancer-promoter interactions to the TSS region of each gene. The vertical lines mark the TSS and the dashed line indicates the cutoff of Cicero score (0.2) used for calculation.

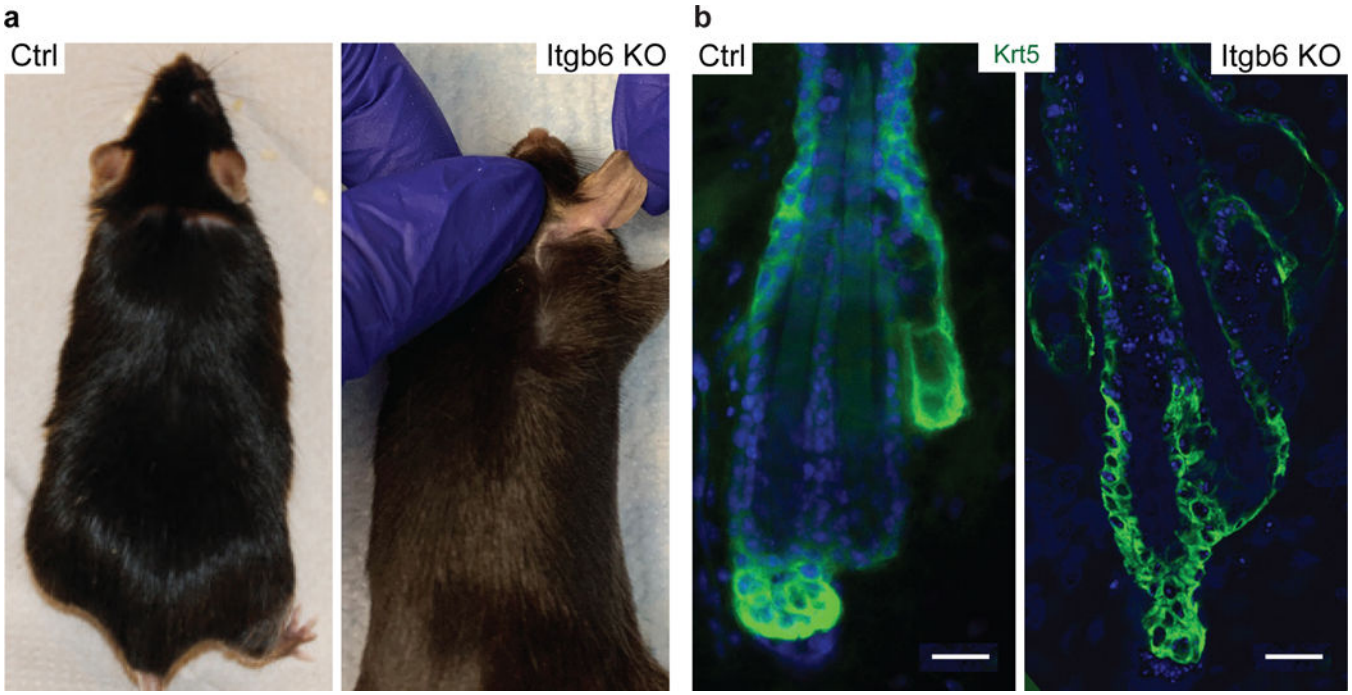

Extended Data Fig. 10. Deletion of *Itgb6* does not lead to premature hair loss.

a, Hair coat is normal in both control and *Itgb6* KO animals at ~9-mo old. **b,** HF-SC compartment is normal in both control and *Itgb6* KO animals at ~9-mo old. Scale bar, 20μm.

Supplementary Material

Refer to Web version on PubMed Central for supplementary material.

Acknowledgements

We thank T. Cech (University of Colorado Boulder, HHMI), K. Green and R. Lavker (Northwestern University) for comments, J. Siegenthaler (University of Colorado School of Medicine) for Foxc1$^{fl/fl}$ and Foxc1-LacZ mouse, E. Fuchs (Rockefeller University, HHMI) for Krt14-H2bGFP and Krt14-Cre mice, D. Sheppard (University of California San Francisco) for Itgb6 KO mice, H. Fujiwara (RIKEN Japan) for NPNT, EGFL6 antibodies, M. Allen (University of Colorado Boulder) for discussing bioinformatic analysis, J. Orth (University of Colorado Boulder), J. Lopez and R. Goldmeyer (Olympus) for two-photon imaging, and all members of the Yi laboratory for suggestions. Research reported in this publication was supported by the National Institute Of Arthritis And Musculoskeletal And Skin Diseases of the National Institutes of Health under Award Number AR059697, AR066703 and AR071435 (to R.Y.). C.Z. was supported by an NCI Predoctoral to Postdoctoral Fellow Transition Award (F99CA253738). The content is solely the responsibility of the authors and does not necessarily represent the official views of the National Institutes of Health.

Data availability

All sequencing data have been deposited to NCBI/GEO SuperSeries under accession number GSE133648.

https://www.ncbi.nlm.nih.gov/geo/query/acc.cgi?acc=GSE133648

References

1. Campisi J. et al. From discoveries in ageing research to therapeutics for healthy ageing. Nature 571, 183–192 (2019). [PubMed: 31292558]
2. López-Otín C., Blasco MA, Partridge L., Serrano M. & Kroemer G. The hallmarks of aging. Cell 153, 1194–1217 (2013). [PubMed: 23746838]
3. Dall'Ara E. et al. Longitudinal imaging of the ageing mouse. Mechanisms of Ageing and Development 160, 93–116 (2016). [PubMed: 27530773]
4. Pittet MJ & Weissleder R. Intravital Imaging. Cell 147, 983–991 (2011). [PubMed: 22118457]
5. Florian MC et al. A canonical to non-canonical Wnt signalling switch in haematopoietic stem-cell ageing. Nature 503, 392–396 (2013). [PubMed: 24141946]
6. Ge Y. et al. The aging skin microenvironment dictates stem cell behavior. Proc Natl Acad Sci U S A 117, 5339–5350 (2020). [PubMed: 32094197]
7. Lay K., Kume T. & Fuchs E. FOXC1 maintains the hair follicle stem cell niche and governs stem cell quiescence to preserve long-term tissue-regenerating potential. Proc. Natl. Acad. Sci. U.S.A. 113, E1506–1515 (2016). [PubMed: 26912458]
8. Matsumura H. et al. Hair follicle aging is driven by transepidermal elimination of stem cells via COL17A1 proteolysis. Science 351, aad4395–aad4395 (2016).
9. Sinha M. et al. Restoring Systemic GDF11 Levels Reverses Age-Related Dysfunction in Mouse Skeletal Muscle. Science 344, 649–652 (2014). [PubMed: 24797481]
10. Wang L., Siegenthaler JA, Dowell RD & Yi R. Foxc1 reinforces quiescence in self-renewing hair follicle stem cells. Science 351, 613–617 (2016). [PubMed: 26912704]
11. Rossi DJ et al. Deficiencies in DNA damage repair limit the function of haematopoietic stem cells with age. Nature 447, 725–729 (2007). [PubMed: 17554309]
12. Janzen V. et al. Stem-cell ageing modified by the cyclin-dependent kinase inhibitor p16INK4a. Nature 443, 421–426 (2006). [PubMed: 16957735]
13. Sharpless NE & DePinho RA How stem cells age and why this makes us grow old. Nat. Rev. Mol. Cell Biol. 8, 703–713 (2007). [PubMed: 17717515]
14. Cheung TH & Rando TA Molecular regulation of stem cell quiescence. Nat Rev Mol Cell Biol 14, 329–340 (2013). [PubMed: 23698583]
15. Cho IJ et al. Mechanisms, Hallmarks, and Implications of Stem Cell Quiescence. Stem Cell Reports 12, 1190–1200 (2019). [PubMed: 31189093]
16. Nakamura-Ishizu A., Takizawa H. & Suda T. The analysis, roles and regulation of quiescence in hematopoietic stem cells. Development 141, 4656–4666 (2014). [PubMed: 25468935]
17. Yi R. Concise Review: Mechanisms of Quiescent Hair Follicle Stem Cell Regulation. Stem Cells 35, 2323–2330 (2017). [PubMed: 28856849]
18. Cheng T. et al. Hematopoietic stem cell quiescence maintained by p21cip1/waf1. Science 287, 1804–1808 (2000). [PubMed: 10710306]
19. Chakkalakal JV, Jones KM, Basson MA & Brack AS The aged niche disrupts muscle stem cell quiescence. Nature 490, 355–360 (2012). [PubMed: 23023126]
20. Tomasetti C. & Vogelstein B. Variation in cancer risk among tissues can be explained by the number of stem cell divisions. Science 347, 78–81 (2015). [PubMed: 25554788]
21. Garza LA et al. Prostaglandin D2 inhibits hair growth and is elevated in bald scalp of men with androgenetic alopecia. Sci Transl Med 4, 126ra34 (2012).
22. Shimomura Y. et al. APCDD1 is a novel Wnt inhibitor mutated in hereditary hypotrichosis simplex. Nature 464, 1043–1047 (2010). [PubMed: 20393562]
23. Pineda CM et al. Intravital imaging of hair follicle regeneration in the mouse. Nat Protoc 10, 1116–1130 (2015). [PubMed: 26110716]
24. Rompolas P. et al. Live imaging of stem cell and progeny behaviour in physiological hair-follicle regeneration. Nature 487, 496–499 (2012). [PubMed: 22763436]
25. Chen C-C et al. Regenerative hair waves in aging mice and extra-follicular modulators follistatin, dkk1, and sfrp4. J Invest Dermatol 134, 2086–2096 (2014). [PubMed: 24618599]

26. Stuart T. et al. Comprehensive Integration of Single-Cell Data. Cell 177, 1888–1902.e21 (2019). [PubMed: 31178118]
27. Salzer MC et al. Identity Noise and Adipogenic Traits Characterize Dermal Fibroblast Aging. Cell 175, 1575–1590.e22 (2018). [PubMed: 30415840]
28. Fujiwara H. et al. The basement membrane of hair follicle stem cells is a muscle cell niche. Cell 144, 577–589 (2011). [PubMed: 21335239]
29. Cao J. et al. The single-cell transcriptional landscape of mammalian organogenesis. Nature 566, 496–502 (2019). [PubMed: 30787437]
30. Lee J. et al. Runx1 and p21 synergistically limit the extent of hair follicle stem cell quiescence in vivo. Proc. Natl. Acad. Sci. U.S.A. 110, 4634–4639 (2013). [PubMed: 23487742]
31. Osorio KM et al. Runx1 modulates developmental, but not injury-driven, hair follicle stem cell activation. Development 135, 1059–1068 (2008). [PubMed: 18256199]
32. Horsley V., Aliprantis AO, Polak L., Glimcher LH & Fuchs E. NFATc1 balances quiescence and proliferation of skin stem cells. Cell 132, 299–310 (2008). [PubMed: 18243104]
33. Keyes BE et al. Nfatc1 orchestrates aging in hair follicle stem cells. Proc. Natl. Acad. Sci. U.S.A. 110, E4950–4959 (2013). [PubMed: 24282298]
34. Lien W-H et al. In vivo transcriptional governance of hair follicle stem cells by canonical Wnt regulators. Nat. Cell Biol. 16, 179–190 (2014). [PubMed: 24463605]
35. Besson V. et al. PW1 gene/paternally expressed gene 3 (PW1/Peg3) identifies multiple adult stem and progenitor cell populations. Proc Natl Acad Sci U S A 108, 11470–11475 (2011). [PubMed: 21709251]
36. Kimura-Ueki M. et al. Hair cycle resting phase is regulated by cyclic epithelial FGF18 signaling. J. Invest. Dermatol. 132, 1338–1345 (2012). [PubMed: 22297635]
37. Plikus MV et al. Cyclic dermal BMP signalling regulates stem cell activation during hair regeneration. Nature 451, 340–344 (2008). [PubMed: 18202659]
38. Hsu Y-C, Li L. & Fuchs E. Transit-amplifying cells orchestrate stem cell activity and tissue regeneration. Cell 157, 935–949 (2014). [PubMed: 24813615]
39. Zhang YV, Cheong J., Ciapurin N., McDermitt DJ & Tumbar T. Distinct self-renewal and differentiation phases in the niche of infrequently dividing hair follicle stem cells. Cell Stem Cell 5, 267–278 (2009). [PubMed: 19664980]
40. Tumbar T. et al. Defining the epithelial stem cell niche in skin. Science 303, 359–363 (2004). [PubMed: 14671312]
41. Blanpain C., Lowry WE, Geoghegan A., Polak L. & Fuchs E. Self-renewal, multipotency, and the existence of two cell populations within an epithelial stem cell niche. Cell 118, 635–648 (2004). [PubMed: 15339667]
42. Morris RJ et al. Capturing and profiling adult hair follicle stem cells. Nat Biotech 22, 411–417 (2004).
43. Adam RC et al. Pioneer factors govern super-enhancer dynamics in stem cell plasticity and lineage choice. Nature 521, 366–370 (2015). [PubMed: 25799994]
44. Nowak JA, Polak L., Pasolli HA & Fuchs E. Hair follicle stem cells are specified and function in early skin morphogenesis. Cell Stem Cell 3, 33–43 (2008). [PubMed: 18593557]
45. Vidal VP et al. Sox9 is essential for outer root sheath differentiation and the formation of the hair stem cell compartment. Curr Biol 15, 1340–51 (2005). [PubMed: 16085486]
46. Buenrostro JD et al. Single-cell chromatin accessibility reveals principles of regulatory variation. Nature 523, 486–490 (2015). [PubMed: 26083756]
47. Buenrostro JD, Giresi PG, Zaba LC, Chang HY & Greenleaf WJ Transposition of native chromatin for fast and sensitive epigenomic profiling of open chromatin, DNA-binding proteins and nucleosome position. Nat Meth 10, 1213–1218 (2013).
48. Naik S. et al. Inflammatory memory sensitizes skin epithelial stem cells to tissue damage. Nature 550, 475–480 (2017). [PubMed: 29045388]
49. Rhee H., Polak L. & Fuchs E. Lhx2 maintains stem cell character in hair follicles. Science 312, 1946–1949 (2006). [PubMed: 16809539]

50. Fan X. et al. Single Cell and Open Chromatin Analysis Reveals Molecular Origin of Epidermal Cells of the Skin. Dev. Cell 47, 21–37.e5 (2018). [PubMed: 30220568]
51. Kadaja M. et al. SOX9: a stem cell transcriptional regulator of secreted niche signaling factors. Genes Dev. 28, 328–341 (2014). [PubMed: 24532713]
52. Klein RH et al. GRHL3 binding and enhancers rearrange as epidermal keratinocytes transition between functional states. PLoS Genet. 13, e1006745 (2017). [PubMed: 28445475]
53. de Guzman Strong C. et al. Lipid defect underlies selective skin barrier impairment of an epidermal-specific deletion of Gata-3. J. Cell Biol. 175, 661–670 (2006). [PubMed: 17116754]
54. Pliner HA et al. Cicero Predicts cis-Regulatory DNA Interactions from Single-Cell Chromatin Accessibility Data. Mol. Cell 71, 858–871.e8 (2018). [PubMed: 30078726]
55. Huang XZ et al. Inactivation of the integrin beta 6 subunit gene reveals a role of epithelial integrins in regulating inflammation in the lung and skin. J. Cell Biol. 133, 921–928 (1996). [PubMed: 8666675]
56. Trempus CS et al. CD34 Expression by Hair Follicle Stem Cells Is Required for Skin Tumor Development in Mice. Cancer Res 67, 4173–4181 (2007). [PubMed: 17483328]
57. Lay K. et al. Stem cells repurpose proliferation to contain a breach in their niche barrier. Elife 7, (2018).

References

1. Driskell RR et al. Distinct fibroblast lineages determine dermal architecture in skin development and repair. Nature 504, 277–281 (2013). [PubMed: 24336287]
2. Corces MR et al. An improved ATAC-seq protocol reduces background and enables interrogation of frozen tissues. Nat. Methods 14, 959–962 (2017). [PubMed: 28846090]
3. Rompolas P. et al. Live imaging of stem cell and progeny behaviour in physiological hair-follicle regeneration. Nature 487, 496–499 (2012). [PubMed: 22763436]
4. Pineda CM et al. Intravital imaging of hair follicle regeneration in the mouse. Nat. Protoc. 10, 1116–1130 (2015). [PubMed: 26110716]
5. Kim D., Langmead B. & Salzberg SL HISAT: a fast spliced aligner with low memory requirements. Nat. Methods 12, 357–360 (2015). [PubMed: 25751142]
6. Li H. et al. The Sequence Alignment/Map format and SAMtools. Bioinforma. Oxf. Engl. 25, 2078–2079 (2009).
7. Anders S., Pyl PT & Huber W. HTSeq--a Python framework to work with high-throughput sequencing data. Bioinforma. Oxf. Engl. 31, 166–169 (2015).
8. Love MI, Huber W. & Anders S. Moderated estimation of fold change and dispersion for RNA-seq data with DESeq2. Genome Biol. 15, 550 (2014). [PubMed: 25516281]
9. Zhou Y. et al. Metascape provides a biologist-oriented resource for the analysis of systems-level datasets. Nat. Commun. 10, 1523 (2019). [PubMed: 30944313]
10. Stuart T. et al. Comprehensive Integration of Single-Cell Data. Cell 177, 1888–1902.e21 (2019). [PubMed: 31178118]
11. Butler A., Hoffman P., Smibert P., Papalexi E. & Satija R. Integrating single-cell transcriptomic data across different conditions, technologies, and species. Nat. Biotechnol. 36, 411–420 (2018). [PubMed: 29608179]
12. Wolf FA, Angerer P. & Theis FJ SCANPY: large-scale single-cell gene expression data analysis. Genome Biol. 19, 15 (2018). [PubMed: 29409532]
13. Cao J. et al. The single-cell transcriptional landscape of mammalian organogenesis. Nature 566, 496–502 (2019). [PubMed: 30787437]
14. Langmead B. & Salzberg SL Fast gapped-read alignment with Bowtie 2. Nat. Methods 9, 357–359 (2012). [PubMed: 22388286]
15. Zhang Y. et al. Model-based Analysis of ChIP-Seq (MACS). Genome Biol. 9, R137 (2008). [PubMed: 18798982]

16. Heinz S. et al. Simple Combinations of Lineage-Determining Transcription Factors Prime cis-Regulatory Elements Required for Macrophage and B Cell Identities. Mol. Cell 38, 576–589 (2010). [PubMed: 20513432]
17. Bailey TL et al. MEME SUITE: tools for motif discovery and searching. Nucleic Acids Res 37, W202–W208 (2009). [PubMed: 19458158]
18. Quinlan AR & Hall IM BEDTools: a flexible suite of utilities for comparing genomic features. Bioinforma. Oxf. Engl. 26, 841–842 (2010).
19. Robinson JT et al. Integrative genomics viewer. Nat. Biotechnol. 29, 24–26 (2011). [PubMed: 21221095]
20. Pliner HA et al. Cicero Predicts cis-Regulatory DNA Interactions from Single-Cell Chromatin Accessibility Data. Mol. Cell 71, 858–871.e8 (2018). [PubMed: 30078726]
21. Ye T. et al. seqMINER: an integrated ChIP-seq data interpretation platform. Nucleic Acids Res. 39, e35 (2011). [PubMed: 21177645]

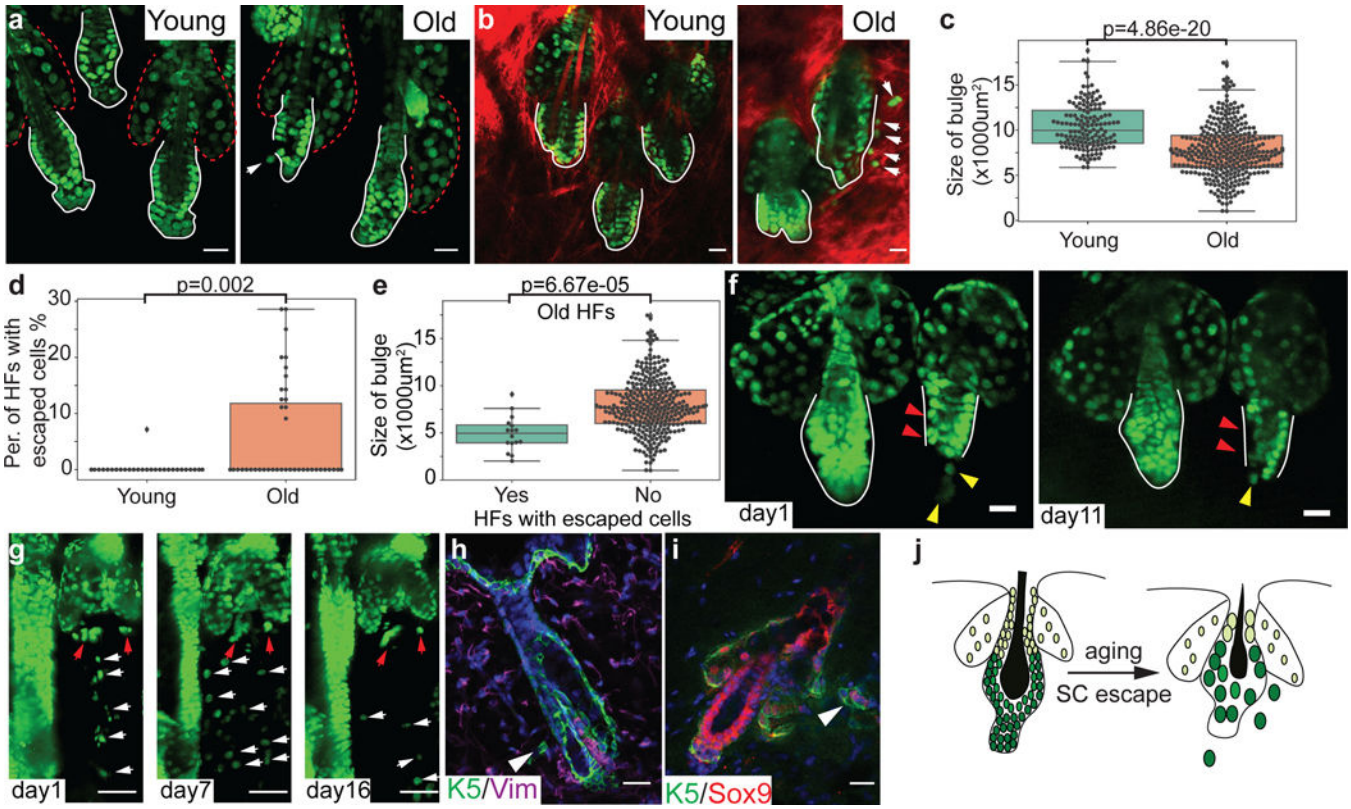

Figure 1. Ageing HFs are characterized by escaped epithelial cells.

a–**b**, Two-photon intravital imaging of young (P42) and old (20mo) HFs. White arrows point to cells of outside of the HF-SC compartment. Red dashed lines outline the SG. White lines outline the HF-SC compartment. Red signals in (**b)** are second-harmonic-generation from collagen fiber in the dermis. Scale bar, 20μm. **c**, Boxplot of the size of HF bulge region. (mean ± s.d.=10423.62 ± 2514.43 (young), 7736.71 ± 2913.99 (old); n=205 HFs, 5 young mice; n=327 HFs, 3 old mice). **d**, Boxplot of the percentage of HFs containing escaped epithelial cells. (mean ± s.d.=0.25 ± 1.3 (young), 5.6 ± 8.9 (old); n=205 HFs, 5 young mice; n=327 HFs, 3 old mice). **e**, Boxplot of the size of HF bulge region, classified based on whether HFs containing escaped cells or not. (mean ± s.d.= 4933.35 ± 1864.29 (escape), 7883.78±2886.42 (no escape); n=327 HFs, 3 old mice). Boxes span the first to the third quartile with the line inside the box representing the median value. The whiskers show the minimum and maximum values or values up to 1.5-times the interquartile range below or above the first or third quartile if outliers are present. Data are plotted as individual points and considered outliers beyond whiskers. Two-sided t-test for **c**–**e**. **f,** Longitudinal tracking of the same HFs in old mice (20mo). Red arrowheads point to epithelial cells in the bulge region, which disappear during the tracking. Yellow arrowheads point to escaped cells outside of HF-SC compartment. White lines outline the bulge region. Scale bar, 20μm. **g**, Longitudinal tracking of a rapidly miniaturized HF in old mice (20mo). White arrows point to escaped epithelial cells in the dermis; red arrows point to the miniaturized HF. Scale bar, 50μm. **h**, Immunofluorescence signals of an old HF (24mo). Arrowhead points to a KRT5+ epithelial cell near the bulge region in the dermis. Scale bar, 20μm. **i,** Immunofluorescence signals of an old HF (24mo). Arrowhead points to KRT5+/Sox9+ epithelial cells near the

bulge region in the dermis. Scale bar, 20μm. **j**, Illustration of HF ageing accompanied by escaped cells.

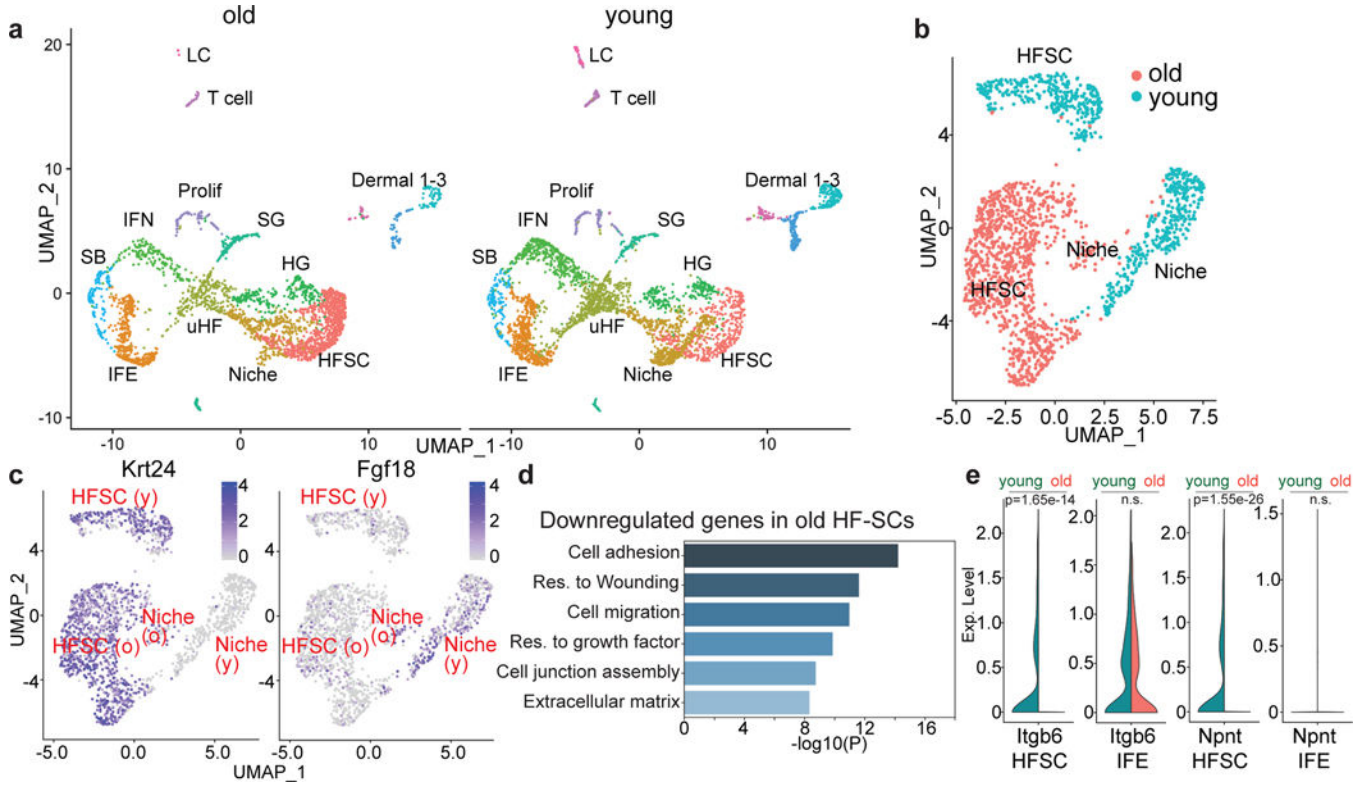

Figure 2. Single-Cell RNA-seq reveals reduced cell adhesion in aged HF-SCs.

a, UMAP clustering of skin cells from old (left) and young (right) mice. Major cell types are classified using marker genes and color-coded with cell identity. HF-SC, hair follicle stem cell; IFE, interfollicular epidermis; uHF, upper hair follicle region; IFN, infundibulum; HG, hair germ; SG, sebaceous gland; Dermal1–3, 3 dermal populations; SB, suprabasal cells; Prolif, proliferating cells; LC, Langerhans cells. **b**, UMAP re-clustering of HF-SCs and niche cells in old and young mice. **c**, Feature plots of marker genes for HF-SC (*Krt24*) and inner bulge niche (*Fgf18*) in old and young samples. **d**, Highly enriched GO terms of downregulated genes in old HF-SCs. **e**, Violin plots of selected cell adhesion and ECM genes in HF-SCs and IFE. Non-parametric Wilcoxon rank sum test.

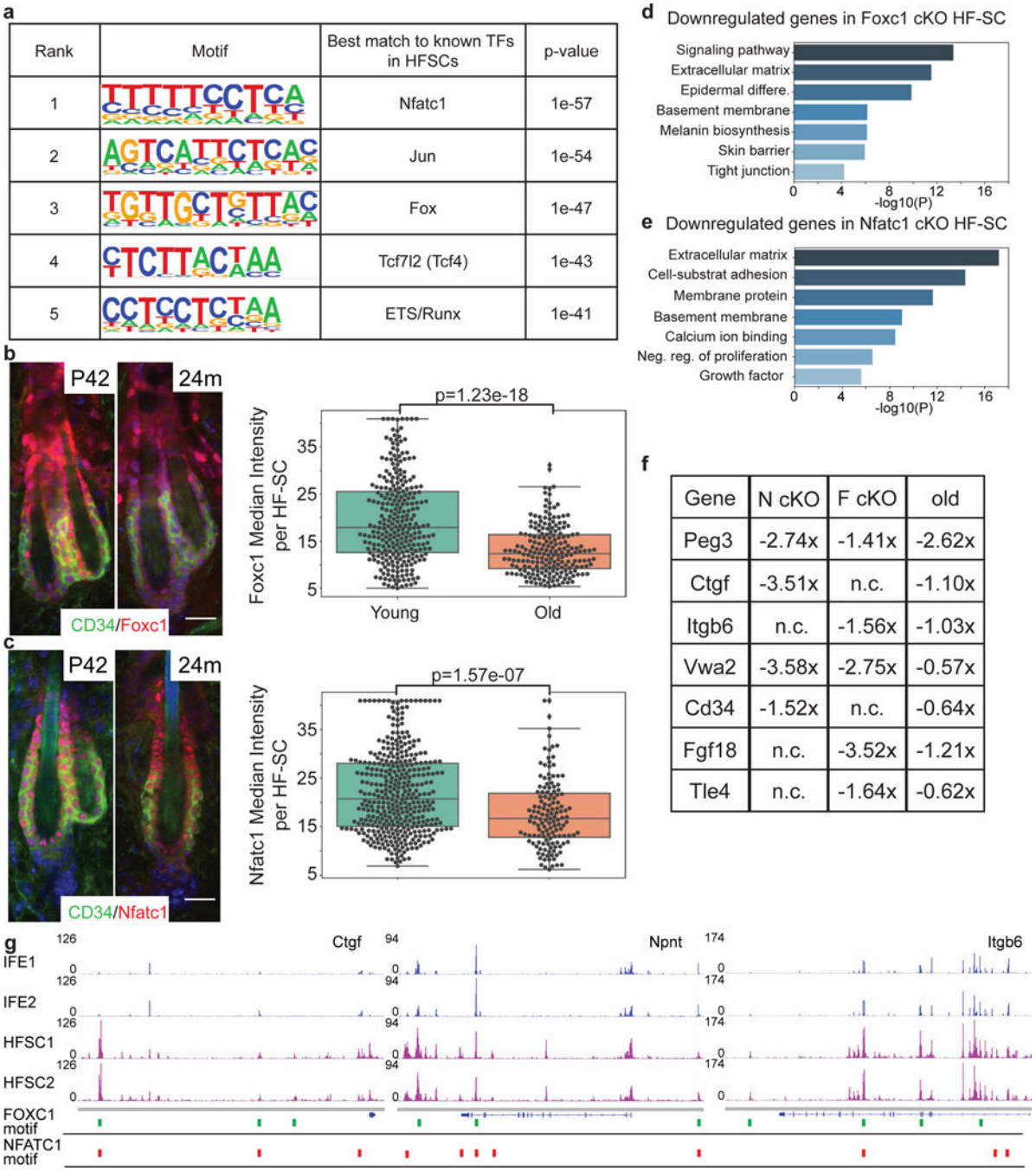

Figure 3. Downregulation of *Foxc1* and *Nfatc1* in aged HF-SCs.

a, Top enriched TF motifs in HF-SC specific open chromatin regions surrounding downregulated genes in aged HF-SCs. Hypergeometric test. **b–c**, Immunofluorescence signals and quantification of FOXC1 and NFATC1 in CD34+ HF-SCs in young (P42) and 24mo old HFs. Scale bar, 20μm. Representative images from n=5 young mice and n=3 old mice. For FOXC1 signal intensity, mean ± s.d.= 1957.39 ± 902.23 (young), 1312.08 ± 512.08 (old). For NFATC1 signal intensity, mean ± s.d.= 2198.63± 845.53 (young), 1770.26± 718.86 (old). Boxes span the first to the third quartile with the line inside the

box representing the median value. The whiskers show the minimum and maximum values or values up to 1.5-times the interquartile range below or above the first or third quartile if outliers are present. Data are plotted as individual points and considered outliers beyond whiskers. Two-sided t-test. **d-e**, Highly enriched GO terms of downregulated genes in *Foxc1* cKO HF-SCs (**d**) and *Nfatc1* cKO HF-SCs (**e**). Hypergeometric test with Benjamini-Hochberg p-value. **f**, HF-SC-enriched cell adhesion and ECM genes and their expression change in each cKO and old mice. N cKO: *Nfatc1* cKO; F cKO: *Foxc1* cKO. n.c., no change. Wald test, statistical value is shown in Supplementary Table 5. **g**, ATAC-seq tracks of *Ctgf*, *Npnt* and *Itgb6* loci in IFE and HF-SC, annotated with FOXC1 (green marks) and NFATC1 (red marks) motifs. ATAC-seq data are normalized and displayed at the same scale across all samples.

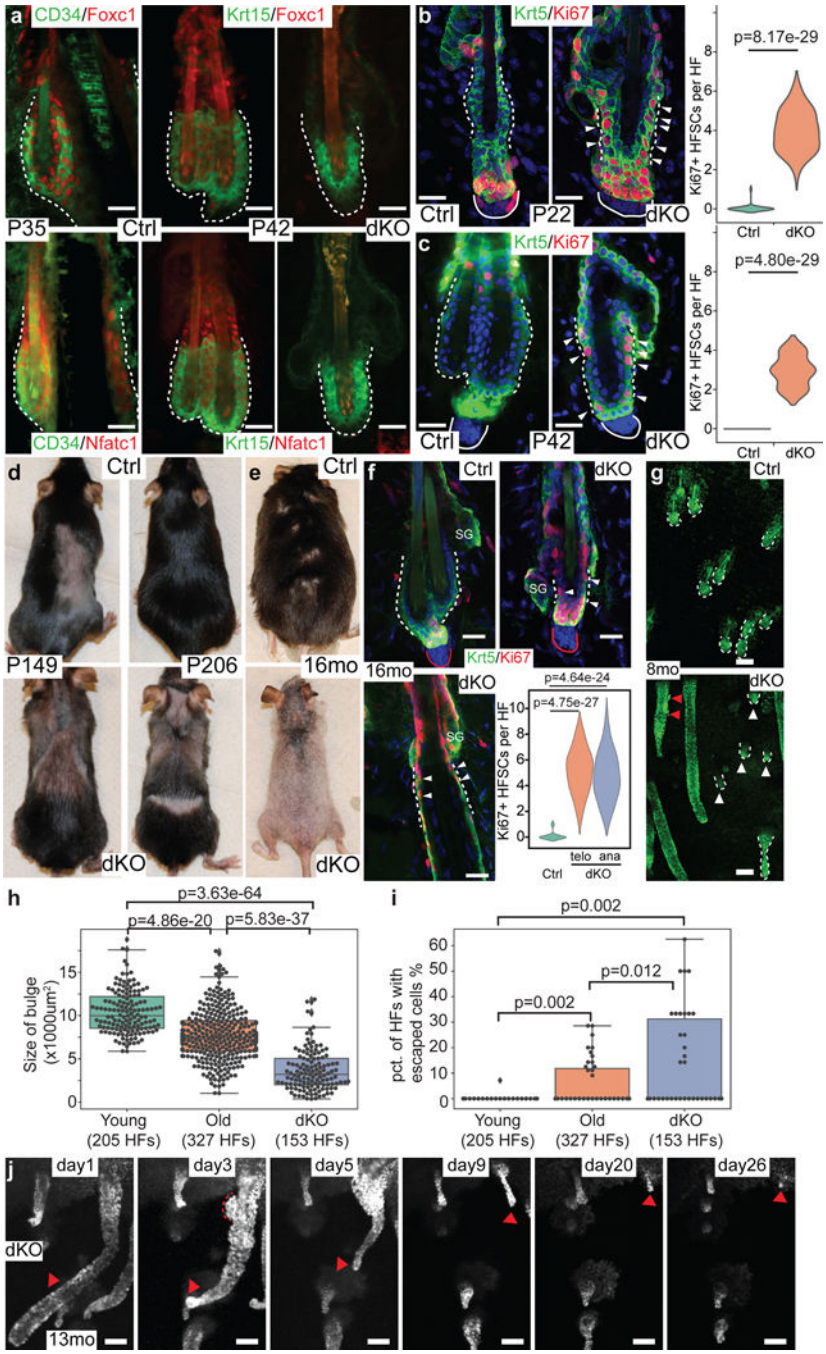

Figure 4. Genetic deletion of *Foxc1* and Nfatc1 causes premature hair loss.

a, Immunofluorescence signals of *Foxc1* and *Nfatc1* expression in HF-SC compartment of late anagen (left, marked by CD34), early telogen (middle, marked by *Krt15*) and in dKO (right, marked by Krt15). Scale bar, 20μm. **b-c**, Staining and quantification of Ki67+ cells in HF-SC compartment in early anagen (**b**) and early telogen (**c**). White arrowheads indicate Ki67+ HF-SCs. (n=30 HFs each from 3 pairs of mice). Scale bar, 20μm. **d-e**, Premature hair loss and graying in dKO by 5mo old (**d**) and 16mo old (**e**) (n>=5 pairs of mice for each time point). **f**, Krt5 and Ki67 staining in control (telogen) and dKO (telogen and anagen) HFs in

16mo old (n=30 HFs each from 3 pairs of mice). White arrowheads indicate Ki67+ HF-SCs. White dashed lines indicate the bulge region. Red lines indicate the dermal papillae. SG, sebaceous gland. Scale bar, 20μm. **g**, Two-photon intravital imaging of HFs in control and dKO mice (8mo), white arrowheads denote miniaturized HFs and red arrowheads mark escaping epithelial cells (n>5 pairs of mice). Scale bar, 70μm. **h**, Boxplot of the size of HF bulge region. (mean ± s.d.=10423.62± 2514.43 (young), 7736.71± 2913.99 (old), 3705.76± 2420.97 (dKO); n=205 HFs, 5 young mice; n=327 HFs, 3 old mice; n=153 HFs, 5 dKO mice). **i**, Boxplot of the percentage of HFs containing escaped epithelial cells. (mean ± s.d.= 0.25 ± 1.3 (young), 5.6 ± 8.9 (old), 12.57± 17.20 (dKO); n=205 HFs, 5 young mice; n=327 HFs, 3 old mice; n=153, 5 dKO mice). Boxes span the first to the third quartile with the line inside the box representing the median value. The whiskers show the minimum and maximum values or values up to 1.5-times the interquartile range below or above the first or third quartile if outliers are present. Data are plotted as individual points and considered outliers beyond whiskers. **j**, Longitudinal tracking of the same HFs in dKO. Red arrowhead points to the same, miniaturizing HF. Red dashed line in the day 3 marks escaping epithelial cells near the HF-SC compartment. Only three cells are left in the HF at day26. Scale bar, 70μm. Data in **b,c,f,h,i** are two-sided t-test.

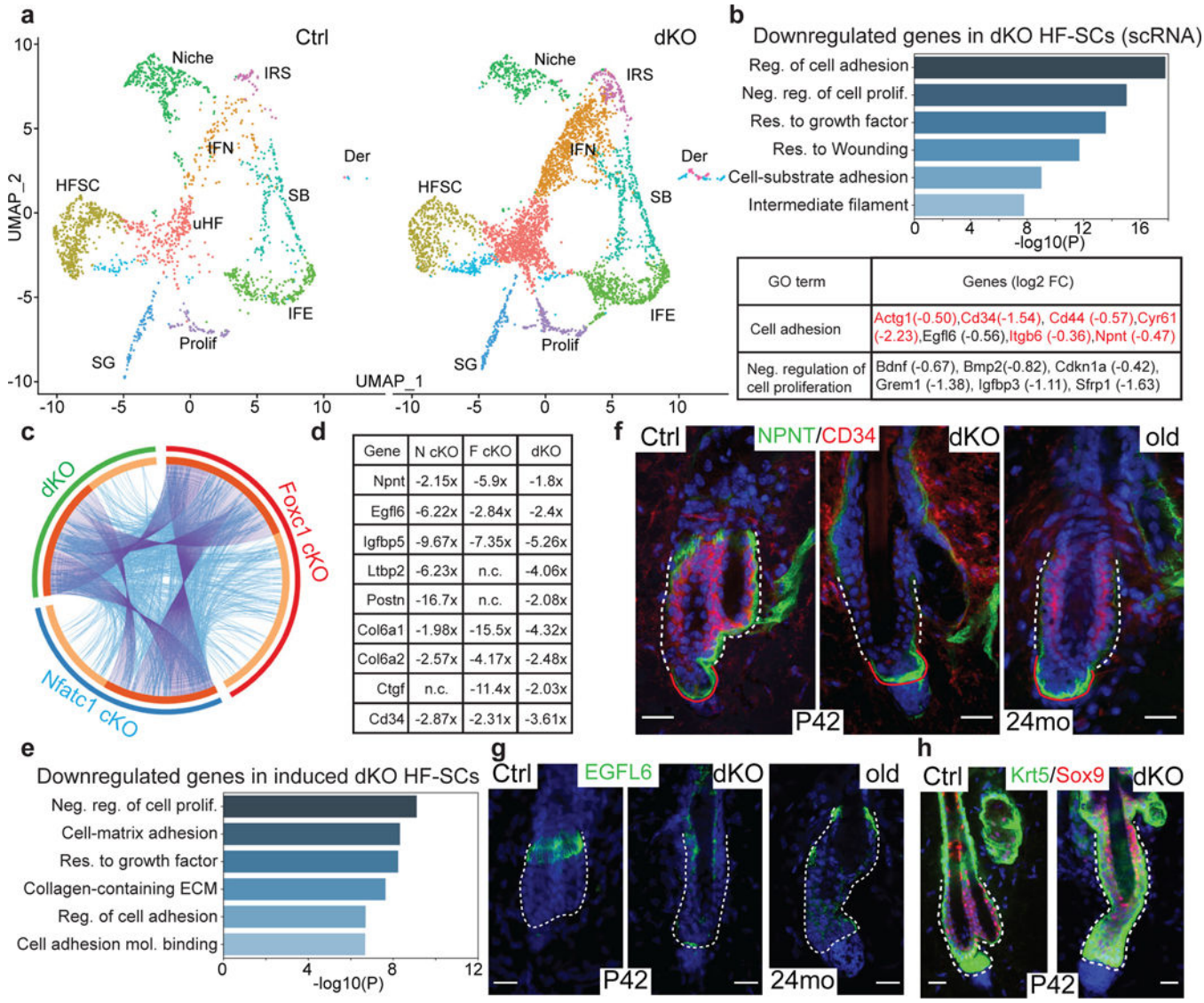

Figure 5. Transcriptomic analysis of dKO HF-SCs.

a, UMAP clustering of control (left) and dKO (right) mouse skin samples. Major cell types are characterized using marker genes and color-coded with cell identity. **b**, Highly enriched GO terms in downregulated genes and selected differentially expressed genes in dKO HF-SCs. Red colored genes are also downregulated in old HF-SCs. **c**, A Circos plot of downregulated genes in *Nfatc1, Foxc1* cKO and induced dKO HF-SCs. Purple curves link identical genes, colored in dark orange, among all three datasets; blue curves link genes that belong to the same enriched GO term among the datasets. Unique genes from each dataset are colored in light orange. **d**, HF-SC-enriched cell adhesion and ECM genes and their expression change in each cKO and induced dKO. n.c., no change. **e**, Highly enriched GO terms in downregulated genes in *Krt15-CrePR*-mediated dKO HF-SCs. **f-g**, Immunofluorescence signals of NPNT, CD34 and EGFL6 in HF-SC compartment in the second telogen (P42) and old mice (representative images from 3 pairs of mice). **h**,

Immunofluorescence signals of SOX9 in control and dKO HFs. Dash lines mark HF-SC compartment. Scale bar, 20μm in f-h.

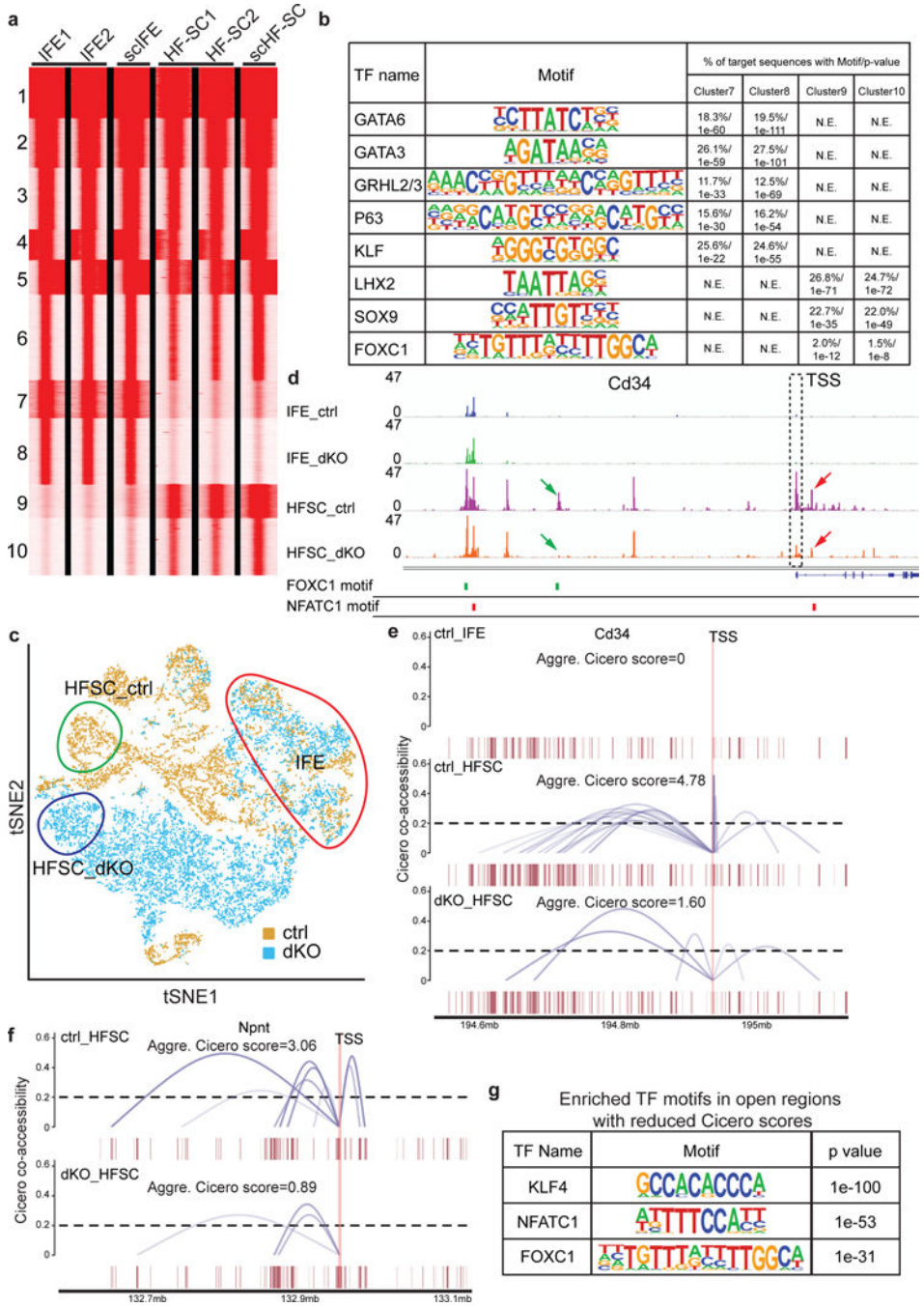

Figure 6. Single-cell open chromatin analysis of HF-SCs reveals the role of *Foxc1* and *Nfatc1*.

a, K-means clustering comparison of open chromatin landscape of purified bulk IFE (IFE1/2), aggregated single-cell IFE (scIFE), purified bulk HF-SC (HF-SC1/2), and aggregated single-cell HF-SC (scHF-SC). **b**, Top enriched TF motifs in clusters 7–10 as classified in (**a**). N.E., not enriched. **c**, T-distributed stochastic neighbor embedding (tSNE) projection of ctrl (light brown) and dKO (blue) epithelial cell lineages based on scATAC-seq data. Circled populations are validated as in **a** and cell lineage-specific open chromatin regions. **d**, Aggregated scATAC-seq tracks of the *Cd34* locus annotated with FOXC1 and

NFATC1 motifs. Locations of FOXC1 (green marks) and NFATC1 (red marks) motifs are indicated. Arrows point to HF-SC-specific open chromatin regions that are lost in dKO and dashed rectangle marks the TSS of *Cd34*. **e-f**, Enhancer-promoter interactions of *Cd34* (**e**) and *Npnt* (**f**) are illustrated in control IFE, control HF-SC and dKO HF-SC. The aggregated Cicero score is calculated by the summation of Cicero scores of all enhancer-promoter interactions to the TSS region of each gene. The vertical lines mark the TSS and the dashed line indicates the cutoff of Cicero score (0.2) used for calculation. **g**, Top enriched TF motifs in open chromatin regions that have reduced Cicero scores in dKO, compared to control.

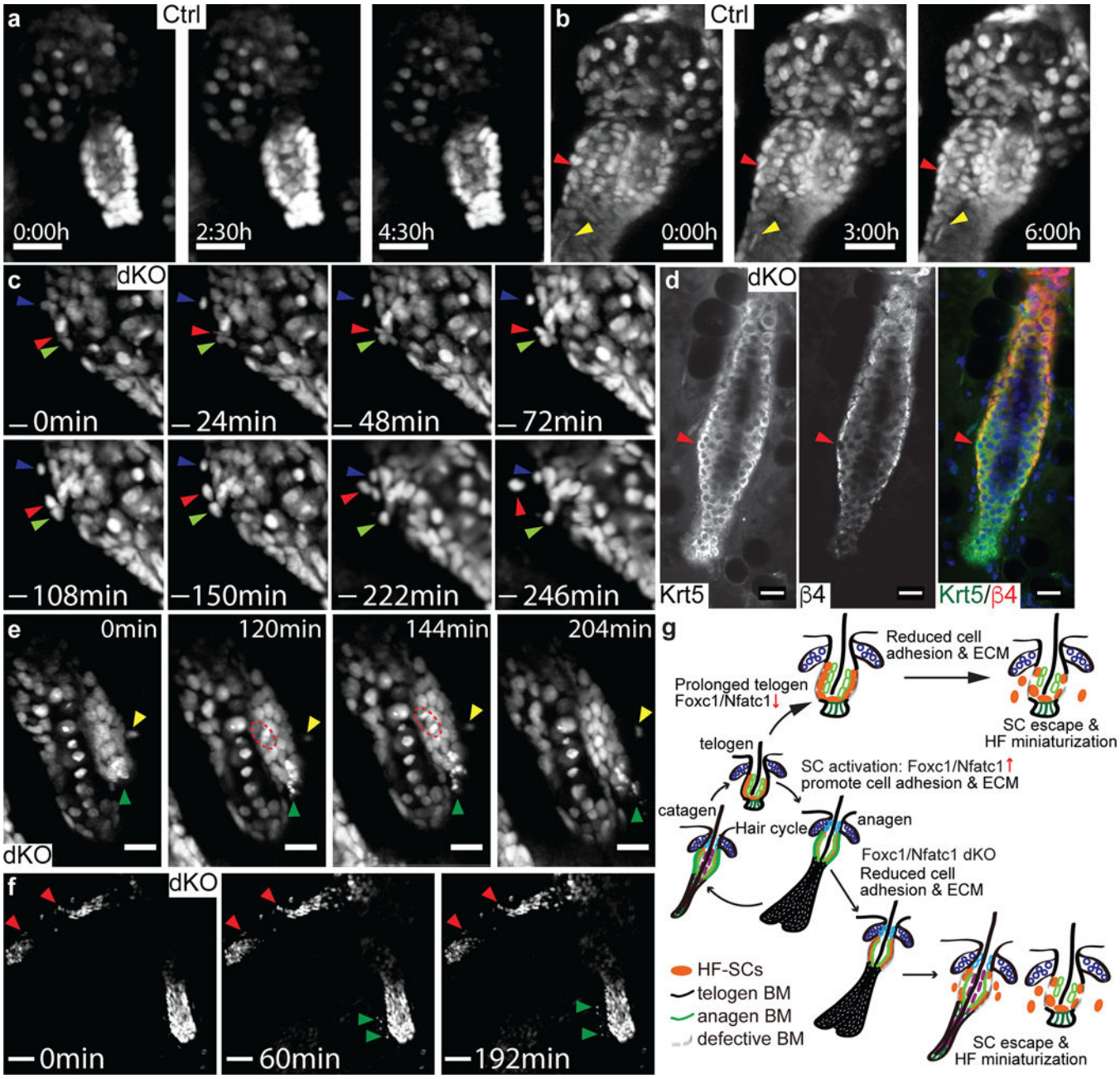

Figure 7. Time-lapse imaging captures HF-SCs escaping from the niche in live animals.

a, Images from a 5-hour movie of telogen HFs in control reveal no cell division and migration in the HF-SC compartment. Scale bar, 30μm. **b**, Images from a 6-hour movie of anagen HFs in control detect migrating HF-SCs and IRS cells. Red arrowhead indicates a downwardly migrating HF-SC and yellow arrowhead indicates an upwardly migrating IRS cell. Scale bar, 30μm. **c**, Images from a 4-hour movie of catagen HFs in dKO detect HF-SCs escaping from the bulge. Blue arrowhead indicates an HF-SC detaching from the bulge, red and green arrowheads indicate two HF-SCs squeezing through the basement membrane and escaping from the bulge region. Note the changed shape of nuclei during the escape. Scale bar, 10μm. **d**, Immunofluorescence signals of β4 integrin in dKO HFs.

Arrowhead point to disrupted basement membrane with the loss of integrin staining. Scale bar, 20μm. **e**, Images from a 3.5-hour movie of a miniaturized hair follicle in dKO reveal the disintegration of HF-SCs, a cell division event and an escaped cell migrating in the dermis. Green arrowheads indicate two disintegrating cells in the miniaturized HF, red dashed circle indicates a dividing cell and yellow arrowhead indicates a migrating cell in the dermis. Scale bar, 20μm. **f**, Images from a 3.2-hour movie of a dying HF and a miniaturizing HF in dKO. Red arrowheads point to escaped epithelial cells with minimum activities in the dermis. Green arrowhead points to rapidly escaping cells from a miniaturizing HF. Scale bar, 50μm. **g,** A model illustrates HF-SC escape and HF miniaturization during ageing and in the dKO HF-SC compartment.